Deducing Electron Properties from Hard X-ray Observations

**E.P. Kontar · J.C. Brown · A.G. Emslie · W. Hajdas ·
G.D. Holman · G.J. Hurford · J. Kašparová ·
P.C.V. Mallik · A.M. Massone · M.L. McConnell ·
M. Piana · M. Prato · E.J. Schmahl · E. Suarez-Garcia**

Abstract X-radiation from energetic electrons is the prime diagnostic of flare-accelerated electrons. The observed X-ray flux (and polarization state) is fundamentally a convolution of the cross-section for the hard X-ray emission process(es) in question with the electron distribution function, which is in turn a function of energy, direction, spatial location and time. To address the problems of particle propagation and acceleration one needs to infer as much information as possible on this electron distribution function, through a deconvolution of this fundamental relationship. This review presents recent progress toward this goal using

E.P. Kontar (✉) · J.C. Brown · P.C.V. Mallik
Department of Physics and Astronomy, University of Glasgow, Kelvin Building, Glasgow, G12 8QQ, UK
e-mail: eduard@astro.gla.ac.uk

A.G. Emslie
Department of Physics, Oklahoma State University, Stillwater, OK 74078, USA

A.G. Emslie
Western Kentucky University, 1906 College Heights Blvd., Bowling Green, KY 42101, USA

W. Hajdas · E. Suarez-Garcia
Paul Scherrer Institut, Villigen PSI, Switzerland

G.D. Holman
NASA Goddard Space Flight Center, Code 671, Greenbelt, MD 20771, USA

G.J. Hurford
Space Sciences Laboratory, University of California, Berkeley, CA 94720, USA

J. Kašparová
Astronomický ústav AV ČR, v.v.i., Fričova 298, Ondřejov, 251 65, Czech Republic

A.M. Massone · M. Prato
CNR-SPIN, Via Dodecaneso 33, 16146 Genova, Italy

M.L. McConnell
Space Science Center, University of New Hampshire, Durham, NH 03824, USA

spectroscopic, imaging and polarization measurements, primarily from the *Reuven Ramaty High Energy Solar Spectroscopic Imager* (*RHESSI*). Previous conclusions regarding the energy, angular (pitch angle) and spatial distributions of energetic electrons in solar flares are critically reviewed. We discuss the role and the observational evidence of several radiation processes: free-free electron-ion, free-free electron-electron, free-bound electron-ion, photoelectric absorption and Compton backscatter (albedo), using both spectroscopic and imaging techniques. This unprecedented quality of data allows for the first time inference of the angular distributions of the X-ray-emitting electrons and improved model-independent inference of electron energy spectra and emission measures of thermal plasma. Moreover, imaging spectroscopy has revealed hitherto unknown details of solar flare morphology and detailed spectroscopy of coronal, footpoint and extended sources in flaring regions. Additional attempts to measure hard X-ray polarization were not sufficient to put constraints on the degree of anisotropy of electrons, but point to the importance of obtaining good quality polarization data in the future.

1 Introduction

X-ray emission, because it is produced promptly in an optically-thin environment, is one of the most direct methods with which to study energetic electrons in solar flares. Such remote radiation measurements are generally functions of photon energy ϵ, direction $\mathbf{\Omega}$, and time t. A common description of incoherent and partially polarized X-ray radiation typical of solar flares is in terms of its *photon intensity* $I(\epsilon, \mathbf{\Omega}, t)$ (photons s^{-1} cm^{-2} sr^{-1} keV^{-1}; CGS units are used throughout the paper) and the fractional degree and orientation of linear polarization (P, Ψ). The emergent photon intensity is the number of photons dN that escape from the source in the time interval t to $t + dt$ in the energy range ϵ to $\epsilon + d\epsilon$, from a solar source with a direction and angular size defined by the elementary cone $d\mathbf{\Omega}$, oriented with respect to the normal of the detector of area dS:

$$dN = I(\epsilon, \mathbf{\Omega}, t) \, d\epsilon \, dS \, d\Omega \, dt. \tag{1.1}$$

For optically-thin radiation, the emergent intensity of the radiation is simply a linear convolution of the cross-section for the pertinent emission process and the electron phase-space distribution function $f_e(\mathbf{v}, \mathbf{r}, t)$ (electrons cm^{-3} [cm s^{-1}]$^{-3}$), or equivalently the particle *flux* $F(E, \mathbf{\Omega}', \mathbf{r}, t)$ (electrons cm^{-2} s^{-1} sr^{-1} keV^{-1}), differential in energy E and velocity solid angle $\mathbf{\Omega}'$. Since $dE = m_e v \, dv$ in the non-relativistic regime, it follows that $F(E, \mathbf{\Omega}', \mathbf{r}, t) = v^2 f_e(\mathbf{v}, \mathbf{r}, t)/m_e$, where m_e (g) is the electron mass.

M. Piana
Dipartimento di Matematica, Universita di Genova, Via Dodecaneso 35, 16146 Genova, Italy

E.J. Schmahl
NWRA/CoRA, Boulder, CO 80301, USA

E. Suarez-Garcia
Department of Nuclear and Particle Physics, University of Geneva, Quai Ernest Ansermet 24, 1212 Geneva, Switzerland

For an elementary bremsstrahlung source of ambient plasma density $n(\mathbf{r})$, located at position $\mathbf{r}$ on the Sun, along the line of sight $\mathbf{\Omega}$, which is subjected to an electron flux spectrum $F(E, \mathbf{\Omega}', \mathbf{r}, t)$, the emergent photon flux spectrum at distance R is the convolution

$$I(\epsilon, \mathbf{\Omega}, t) = \int_\ell \int_{\Omega'} \int_\epsilon^\infty n(\mathbf{r}) F(E, \mathbf{r}, \mathbf{\Omega}', t) Q(\mathbf{\Omega}, \mathbf{\Omega}', \epsilon, E) \, dE \, d\mathbf{\Omega}' \, d\ell, \qquad (1.2)$$

where ℓ is the distance along the line of sight, $Q(\mathbf{\Omega}, \mathbf{\Omega}', \epsilon, E)$ $(\mathrm{cm}^2 \, \mathrm{keV}^{-1} \, \mathrm{sr}^{-1})$ is the cross-section for the pertinent hard X-ray emission process(es), differential in ϵ and $\mathbf{\Omega}$. The dominant hard X-ray emission process in solar flares is *bremsstrahlung* radiation associated with electron deceleration in the Coulomb field of an ion or other electron. For this process, the angular dependence of Q depends only on the angle $\theta' = \overline{\mathbf{\Omega}' \mathbf{\Omega}}$ between the incoming electron $\mathbf{\Omega}'$ and the emitted photon $\mathbf{\Omega}$ directions, so that $Q = Q(\epsilon, E, \theta')$.

To deduce the physical properties of energetic particles in solar flares from observed hard X-ray quantities, the electron flux spectrum $F(E, \mathbf{r}, \mathbf{\Omega}', t)$ must be deconvolved from the emission cross-section $Q(\epsilon, E, \theta')$ in this integral. Although the relation between the observable quantity $I(\epsilon, \mathbf{\Omega}, t)$ and the physical electron flux $F(E, \mathbf{r}, \mathbf{\Omega}', t)$ is linear, it is still nontrivial and the deconvolution requires some rather insightful techniques. This fundamental problem and the progress toward the solution of the problem using spectroscopic, imaging and polarization measurements from the *Reuven Ramaty High Energy Solar Spectroscopic Imager* (*RHESSI*, Lin et al. 2002) are addressed in this review.

In Sect. 2, we review the physical processes leading to X-ray emission in solar flares, including free-free electron-ion bremsstrahlung (Sect. 2.1), free-bound electron-ion emission (Sect. 2.2), and free-free electron-electron bremsstrahlung (Sect. 2.3). This review, however, does not discuss bound-bound transitions, nor the emissions due to energetic ions such as nuclear gamma-ray lines, ion gamma-ray continuum, and pseudo-continuum.

Since the emission mechanisms are well established, hard X-rays (HXRs) are often viewed as one of the most direct (i.e., least affected by propagation effects) diagnostics of solar flare electrons. However, it must not be forgotten that downward-propagating X-ray photons are effectively scattered toward the observer by electrons in the dense layers of the solar atmosphere, thereby complicating the diagnostic potential of hard X-ray radiation. Section 3 reviews spectroscopic and imaging techniques to infer this Compton backscattered (albedo) component. Progress in the deduction of primary, i.e., directly flare-emitted, and photospherically-reflected X-rays from the observed spectrum, is discussed.

Section 4 presents an overview of the results obtained using purely spectroscopic data (i.e., data integrated over the source volume). Both forward fitting and regularized inversion techniques to deduce the energy dependence of the *mean source electron flux spectrum* $\overline{F}(E)$ (averaged over volume and solid angle) are reviewed. Properties of the electron flux distribution, deviations from power-law forms, low-energy cutoffs and interpretation in terms of a thermal source are discussed.

Section 5 provides methods and results for the case of an anisotropic angular distribution $\overline{F}(E, \mathbf{\Omega})$ of electrons. The role of X-ray Compton scattering in the solar atmosphere (solar albedo) in deducing this angular distribution is discussed. Recent *RHESSI* polarization measurements and their implications for electron anisotropy are also reviewed.

Section 6 focuses on the spatial structure $F(E, \mathbf{r})$ of the electron flux, using imaging spectroscopy observations from *RHESSI*. Recently-developed, visibility-based techniques to optimize the inference of electron maps are discussed. Section 7 highlights the major finding from *RHESSI* and discusses the open questions.

The role of these results in the context of multi-wavelength observations of solar flares is discussed by Fletcher et al. (2011, this issue). The implications of these findings for electron

transport, and acceleration models are discussed by Holman et al. (2011, this issue), Hannah et al. (2011, this issue), and Zharkova et al. (2011, this issue).

2 X-ray Emission Processes and Energetic Electrons

When energetic electrons are deflected in close encounters with ambient particles (both electrons and ions), a *bremsstrahlung* (literally, "braking radiation") photon is produced. As stated in Sect. 1, the cross-section $Q(\epsilon, E, \theta')$ for electron-ion free-free bremsstrahlung is a function of the emitted photon energy ϵ, the pre-collision electron energy E, and the angle θ' between the direction of the pre-collision electron and the outgoing photon (see, e.g., Koch and Motz 1959). For simplicity we often consider only the solid-angle-integrated form of the cross-section $Q(\epsilon, E)$ (and the corresponding scalar electron flux $F[E, \mathbf{r}, t]$); however, it must be remarked that the effects of the angular dependence of the cross-section can, for highly-beamed electron distributions, be quite significant, leading to substantial differences in the number of electrons required to produce a given hard X-ray flux—see Sect. 5.

The photons of energy from a few keV to a few hundred keV under consideration are mostly produced by collisional electron-ion bremsstrahlung in the solar atmosphere. Bremsstrahlung emission from energetic electrons is more efficient than inverse Compton scattering or synchrotron emission from the same electron population (Korchak 1967). The responsible electrons have kinetic energies E up to a few hundreds of keV, and so will collisionally stop within a column density $N \approx E^2/6\pi e^4 \Lambda \sim 10^{17} E^2 \lesssim 10^{21}$ cm^{-2}, where e (esu) is the electronic charge and Λ the Coulomb logarithm (e.g., Emslie 1978). Thus, the column density in a solar coronal loop of density 10^{10} cm^{-2} and length 10^9 cm is 10^{19} cm^{-2}, which stops electrons up to $\sim$10 keV, while the upper chromosphere with typical column densities 10^{20}–10^{22} cm^{-2} can stop electrons with the energies 10–300 keV. The cross-section for scattering the emitted photons is of the order of the Compton cross-section $\sigma_C \approx \pi r_o^2 \approx 2 \times 10^{-25}$ cm^2, where $r_o = e^2/m_e c^2$ is the classical electron radius, so that the optical depth $\tau = N\sigma_C \approx 10^{-4}$ and there is negligible self-absorption in the source, i.e., the source is optically thin. In Sect. 3, we shall address the issue of so-called "albedo" photons—photons that are emitted downward toward the solar photosphere, which is optically thick, and subsequently backscattered toward the observer. For now, we consider only "primary" photons, i.e., those initially directed toward the observer. Integrating the photon intensity $I(\epsilon, \Omega)$ over the solid angle subtended by the source of area A, $d\Omega = dA/R^2$ and making the volume element substitution $d\Omega\, d\ell = d^3r/R^2$, the fundamental equation (1.2) shows that the observed bremsstrahlung flux (at time t; hereafter understood) at the Earth (photons s^{-1} keV^{-1} cm^{-2} of detector area) is

$$I(\epsilon) = \frac{1}{4\pi R^2} \int_\epsilon^\infty \int_V n(\mathbf{r})\, F(E, \mathbf{r})\, Q(\epsilon, E)\, dE\, d^3\mathbf{r}, \qquad (2.1)$$

where the second integral is taken over the source volume V.

2.1 Electron-Ion Bremsstrahlung

For electron-ion bremsstrahlung, the full form of the cross-section $Q(\epsilon, E)$ is given by formula 3BN of Koch and Motz (1959). Numerical computations may be facilitated by use of the simplified form published by Haug (1997). A frequently-used analytic approximation to the cross-section $Q(\epsilon, E)$ is the Kramers form

$$Q(\epsilon, E) = Z^2 \frac{\sigma_o}{\epsilon E}, \qquad (2.2)$$

where $\sigma_o = (8\alpha/3)(m_e c^2)r_o^2 = 7.9 \times 10^{-25}$ cm^2 keV. Here $\alpha \simeq 1/137$ is the fine structure constant, m_e is the electron mass, Z is the mean ion charge, c is the speed of light. A more accurate analytic form, valid in the non-relativistic limit, is the Bethe-Heitler form

$$Q(\epsilon, E) = Z^2 \frac{\sigma_o}{\epsilon E} \ln \frac{1 + \sqrt{1 - \epsilon/E}}{1 - \sqrt{1 - \epsilon/E}}. \tag{2.3}$$

For purely spectral observations, a spatially-integrated form of the basic equation (2.1) is appropriate. In this case, we can write (e.g., Brown 1971)

$$I(\epsilon) = \frac{1}{4\pi R^2} \int_\epsilon^\infty [\overline{n} V \overline{F}(E)] \, Q(\epsilon, E) \, dE, \tag{2.4}$$

where $\overline{n} = (1/V) \int_V n(\mathbf{r}) \, d^3\mathbf{r}$ and $\overline{F}(E) = (1/\overline{n}V) \int_V n(\mathbf{r}) F(E, \mathbf{r}) \, d^3\mathbf{r}$. The quantity $\overline{F}(E)$ (electrons cm^{-2} s^{-1} keV^{-1}) is termed the *mean electron flux spectrum* (Brown et al. 2003); it has also been termed the "X-ray emitting electron spectrum" by Johns and Lin (1992a, 1992b). Since the quantity $\overline{n} V$ (the number of target particles in the emitting volume) is dimensionless, the units of the quantity $[\overline{n} V \overline{F}(E)]$ are the same as those for electron flux, viz., electrons cm^{-2} s^{-1} keV^{-1}. For large events, typical values of $\overline{F}(E)$ and $[\overline{n} V \overline{F}(E)]$ at a representative energy $E \simeq 20$ keV are of order 10^{18} and 10^{55}, respectively.

The inference of $[\overline{n} V \overline{F}(E)]$ corresponding to an observed $I(\epsilon)$ may be accomplished in several ways, which are described in detail later in this chapter. A review of the different degrees of effectiveness of these techniques in discerning the overall magnitude of, overall spectral shape of, and form of "local" features in $\overline{F}(E)$ has been presented by Brown et al. (2006).

It is of crucial importance to note that the quantity $[\overline{n} V \overline{F}(E)]$ is the *only* quantity that can be inferred unambiguously (i.e., without additional model assumptions) from the source-integrated bremsstrahlung emission $I(\epsilon)$. Use of (2.4) to obtain $[\overline{n} V \overline{F}(E)]$ for a given $I(\epsilon)$ is therefore a fundamental issue in the interpretation of solar hard X-ray spectra. Once $[\overline{n} V \overline{F}(E)]$ has been determined, the actual magnitude of $\overline{F}(E)$ depends on the values[1] of $\overline{n}$ and V.

As an example of the use of the mean source electron spectrum to determine physical properties of solar flares, let us consider the inference of the *accelerated* electron flux spectrum $\mathcal{F}_0(E_0)$. The bremsstrahlung yield, the number of bremsstrahlung photons emitted between ϵ and $\epsilon + d\epsilon$ from an electron of initial energy E_0 in a plasma of density $n(\mathbf{r})$, may be written

$$\nu(\epsilon, E_0) = \int_\epsilon^{E_0} \frac{n(\mathbf{r}) Q(\epsilon, E) \nu(E) \, dE}{|dE/dt|}, \tag{2.5}$$

where dE/dt is the energy loss rate (here assumed a function of E only). For energy losses in a cold target due to binary collisions with the background electrons (radiation energy losses are much smaller and can be ignored), $dE/dt = -(K/E)n(\mathbf{r})v(E)$, where $K = 2\pi e^4 \Lambda = 2.6 \times 10^{-18}$ cm^2 keV^2 (Emslie 1978), and so the total observed flux from an *injected* distribution with energy spectrum $\mathcal{F}_0(E_0)$ (electrons cm^{-2} s^{-1} keV^{-1}) is

---

[1]The astute reader will note that as the source volume $V \to \infty$, the value of $\overline{F}(E) \to 0$. This formal difficulty may be removed in practice by the truncation of the emission volume V at some reasonable upper limit.

$$I(\epsilon) = \frac{A}{4\pi R^2} \int_{E_0=\epsilon}^{\infty} \mathcal{F}_0(E_0) \nu(\epsilon, E_0) \, dE_0$$

$$= \frac{A}{4\pi R^2} \frac{1}{K} \int_{E_0=\epsilon}^{\infty} \mathcal{F}_0(E_0) \, dE_0 \int_{E=\epsilon}^{E_0} E \, Q(\epsilon, E) \, dE, \quad (2.6)$$

where A (cm^2) is the area of the flare. Reversing the order of integration in (2.6) gives

$$I(\epsilon) = \frac{A}{4\pi R^2} \frac{1}{K} \int_{E=\epsilon}^{\infty} E \, Q(\epsilon, E) \, dE \int_{E_0=E}^{\infty} \mathcal{F}_0(E_0) \, dE_0, \quad (2.7)$$

and comparing this with the fundamental equation (2.4) yields the result

$$\overline{n}V\overline{F}(E) = \frac{A}{K} E \int_{E_0=E}^{\infty} \mathcal{F}_0(E_0) \, dE_0. \quad (2.8)$$

From this it follows straightforwardly that

$$A\mathcal{F}_0(E_0) = -K \frac{d}{dE} \left(\frac{\overline{n}V\overline{F}(E)}{E} \right)_{E=E_0}, \quad (2.9)$$

permitting the determination of the quantity $A\mathcal{F}_0(E_0)$ (electrons s^{-1} keV^{-1}); this quantity represents the *rate* of injection of electrons per unit energy (e.g., Holman et al. 2003). Clearly $\mathcal{F}_0(E_0)$ is a nonnegative function, and so (2.9) constrains $\overline{F}(E)$ to either be a decreasing function of E or, at worst, a function that increases more slowly than E. As we shall see below, certain recovered forms of $[\overline{n}V\overline{F}(E)]$ (e.g., Piana et al. 2003) can have difficulty satisfying this constraint; however it is also shown that such difficulties may be removed if the effects of photospherically-backscattered (albedo) photons (e.g., Kontar et al. 2006) are taken into account in (2.4).

2.2 Free-Bound Emission

In fitting or inferring mean source electron flux spectra $\overline{F}(E)$, free-bound recombination emission by nonthermal electrons had always been neglected compared with free-free electron-ion bremsstrahlung, as argued by Korchak (1967) and Landini et al. (1973). For *hot* plasma hard X-ray sources (coronal or in soft X-ray footpoints) this is inconsistent with inclusion of recombination as significant for thermal electrons of similar energies in thermal spectrum modeling (e.g., Culhane 1969; Culhane and Acton 1970). Of importance also is the fact that the estimated coronal abundance A_Z for Fe is now much higher than in e.g. Landini et al. (1973). The recombination emission rate $\propto Z^4 A_Z$ for hydrogenic ions of charge Ze and abundance A_Z with $A_Z Z^4 \approx 1$ for H and ≈ 40 for Fe^{25+}. Brown et al. (2010) have therefore re-examined the importance of nonthermal electron recombination.

In the hydrogenic Kramers approximation, the free-bound emission rate from a plasma of proton density n_p and volume V from nonthermal electrons with mean source electron spectrum $\overline{F}(E)$ is given by Brown et al. (2010)

$$J_R(\epsilon) \approx \frac{32\pi}{3\sqrt{3}\alpha} \frac{r_e^2 \chi^2}{\epsilon} n_p V \sum_{Z_{\text{eff}}} \sum_{n \geq n_{\min}} \frac{p_n}{n^3} Z_{\text{eff}}^4 A_{Z_{\text{eff}}} \frac{\overline{F}(\epsilon - Z_{\text{eff}}^2 \chi/n^2)}{\epsilon - Z_{\text{eff}}^2 \chi/n^2}, \quad (2.10)$$

where $\chi = 13.6$ eV is the H ionization potential, Z_{eff} the effective charge on the ion, r_e the classical electron radius and α the fine-structure constant. n is the principal quantum number
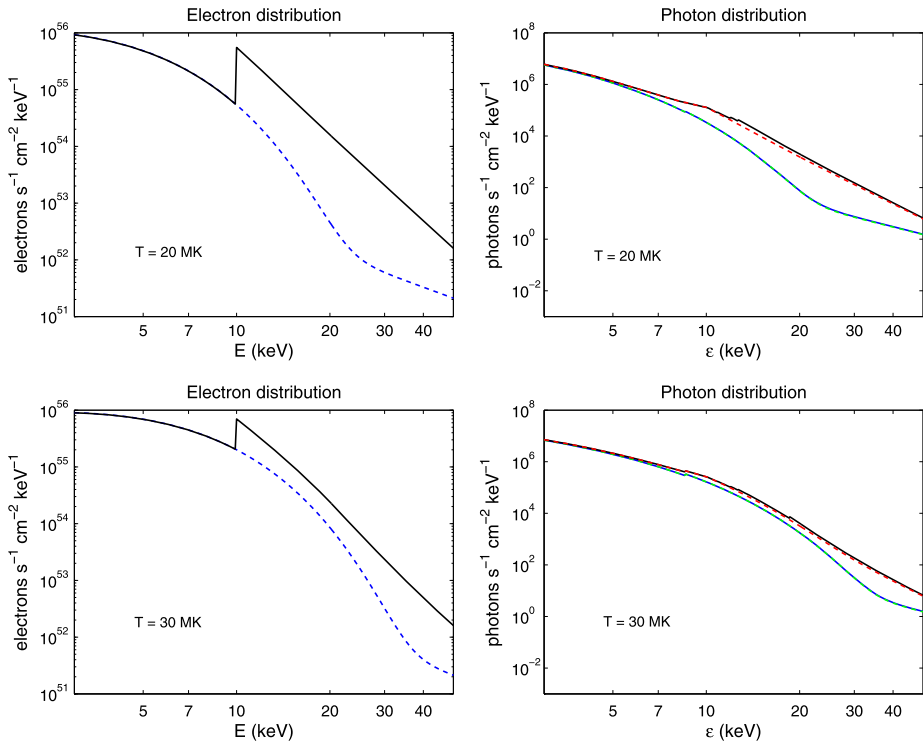
Fig. 1 *Left:* the thin-target (including both thermal and nonthermal) electron and photon (*right*) spectra for two different plasma temperatures, 20 MK (*top*) and 30 MK (*bottom*). Electron nonthermal spectra for various values of low energy cutoff E_c and electron spectral index δ: $E_c = 1$ keV and $\delta = 2$ (*blue and dashed*); $E_c = 10$ keV and $\delta = 5$ (*black and solid*); The corresponding photon spectra: *blue solid line* for $\delta = 2$, $E_c = 1$ keV with free-bound emission; *green dashed line* for $\delta = 2$, $E_c = 1$ keV without free-bound emission; *black solid line* for $\delta = 5$, $E_c = 10$ keV with free-bound; *red dashed line* for $\delta = 5$, $E_c = 10$ keV without free-bound

of the empty shell into which the electron recombines and p_n is a 'vacancy factor' which takes into account the ratio of available to total states in that shell. [Note that (2.10) applies for $\epsilon \geq E_c + Z_{\text{eff}}^2 \chi / n^2$; for $\epsilon < E_c + Z_{\text{eff}}^2 \chi / n^2$, $J_R(\epsilon) = 0$.] Since the recombination cross-section falls off as $1/n^3$, it is adequate to take $n = n_{\min}$, the value for the first empty n-shell. A key feature of free-bound emission, unlike free-free, is that for any specific shell, each electron energy value E maps to a unique photon energy value ϵ so that $J_R(\epsilon)$ is a much more direct reflection of $\overline{F}(E)$ than is the bremsstrahlung $J_B(\epsilon)$ convolution of $\overline{F}(E)$, the former preserving features in $\overline{F}(E)$.

Comparing (2.10) with the corresponding Kramers free-free expression, Brown and Mallik (2008, 2009) concluded that nonthermal free-bound emission is negligible in cold sources. However, they concluded that in hot plasmas ($T \approx 10$–30 MK), such as coronal sources and the soft X-ray component of footpoint sources, free-bound emission can dominate for steep spectra and low cut-off energies (Fig. 1). Subsequently, a serious error in Brown and Mallik (2008, 2009), involving the use of incorrect values of $n_{\min}$ in their equation (13) (i.e., (2.10) above) was recognized (Brown et al. 2010). This substantially reduced both the magnitude of the cross-section and the energy shift $\epsilon - E$ involved in recombination. Because of the typically steep electron spectra involved, the latter substantially affects

the number of electrons responsible for emitting the photon in question. In the amended results $J_R(\epsilon)$ is never dominant, even for hot sources, but can account for up to $\sim 30\%$ of the flux $J_B(\epsilon) + J_R(\epsilon)$ in the range ~ 10–30 keV for the non-thermal component dominating thermal as shown in Fig. 1. *For such hot sources*, the free-bound emission could be comparable with such effects as albedo and differences in bremsstrahlung cross-section used, and could be used to diagnose the sharp features in $\overline{F}(E)$ from $J(\epsilon)$. Even more important is the fact that $J_R(\epsilon)$ adds edges to the total $J(\epsilon)$ with the result that, in data with good signal to noise ratio, inversion (essentially differentiation) of data $J(\epsilon)$ to yield $\overline{F}(E)$ based on bremsstrahlung alone (essentially differentiation of J) could result in spurious features in $\overline{F}(E)$ just as happens when albedo is ignored.

2.3 Electron-Electron Bremsstrahlung

Energetic electrons propagating in the solar atmosphere encounter ions and electrons (both free and bound) and hence can produce X-ray emission via both electron-ion and electron-electron bremsstrahlung.

When the maximum electron energy is much larger than the photon energies under consideration, the photon spectrum resulting from a power-law spectrum of electrons $\overline{F}(E) \propto E^{-\delta}$ is also close to the power-law form $I(\epsilon) \propto \epsilon^{-\gamma}$ (Haug 1989). However, while for pure electron-ion bremsstrahlung $\gamma \simeq \delta + 1$, for pure electron-electron bremsstrahlung a significantly shallower photon spectrum, with $\gamma \simeq \delta$, results. Thus, the importance of the electron-electron bremsstrahlung contribution increases with photon energy and the enhanced emission per electron leads to a flattening of the photon spectrum $I(\epsilon)$ above ~ 300 keV produced by a given $\overline{F}(E)$ (Haug 1975) or, equivalently, a steepening of the $\overline{F}(E)$ form required to produce a given $I(\epsilon)$. Kontar et al. (2007) provide a discussion of the essential differences between electron-electron and electron-ion bremsstrahlung processes. We here provide a succinct summary of that discussion and note that the properties of electrons with the energies above ~ 400 keV are also crucial for ion diagnostics and radio emission.

As is well known (Koch and Motz 1959), the cross-section for electron-ion bremsstrahlung scales as Z^2. Further, when considering electron-electron bremsstrahlung, the possible binding of target electrons to their host ions in a neutral or partially-ionized medium is not significant. Hence, in a quasi-neutral target of particles with atomic number Z, the bremsstrahlung cross-section per atom for emission of a photon of energy ϵ by an electron of energy E is in general equal to

$$Q(\epsilon, E) = Z^2 Q_{e-p}(\epsilon, E) + Z Q_{e-e}(\epsilon, E), \tag{2.11}$$

where $Q_{e-p}(\epsilon, E)$ and $Q_{e-e}(\epsilon, E)$ are the cross-sections, in the laboratory frame, for electron-proton, and electron-electron bremsstrahlung, as given by Koch and Motz (1959) and Haug (1989), respectively.[2] It is also important to note that while the electron-ion cross-section is finite for all $\epsilon < E$, the cross-section for electron-electron bremsstrahlung vanishes above a maximum photon energy, due to the necessarily finite energy carried by the recoiling target electron (Haug 1975; Kontar et al. 2007). For highly *non*-relativistic electrons ($E \ll m_e c^2$), $\epsilon_{\max} \to E/2$; only for highly *relativistic* electrons ($E \gg m_e c^2$) can $\epsilon_{\max} \to E$ (see Fig. 2). As discussed by Kontar et al. (2007), this result has important implications for the form of the photon spectrum produced by electron-electron bremsstrahlung.

In Sect. 4, we discuss the application to the recovery of the electron spectrum at pertinent (mildly-relativistic) energies.

---

[2]Note that there is a typographical error in the form of Q_{e-e} in Haug (1989); see Kontar et al. (2007) for details.
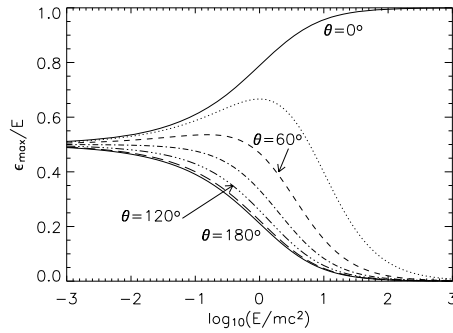
Fig. 2 Maximum photon energy ϵ_{max} produced by electron-electron bremsstrahlung, expressed as a fraction of the incident electron energy E (in units of the electron rest mass mc^2), for various values of θ, the angle between the incoming electron and the outgoing photon trajectories. For clarity, only curves for $\theta = 0°$, $60°$, $120°$, and $180°$ are labeled; the curves for $\theta = 30°$, $90°$ and $150°$ lie between these (after Kontar et al. 2007)

3 Primary and Compton Backscattered X-rays

As discussed in Sect. 2, the atmosphere *above* the X-ray bremsstrahlung-producing region is optically thin. However, the very dense lower photospheric layers *below* the primary source are not. Consequently, photons emitted downwards are efficiently Compton backscattered by atomic electrons in the photosphere. The observed hard X-ray (HXR) flux spectrum from solar flares is therefore a combination of primary bremsstrahlung photons with a spectrally modified component from photospheric Compton backscatter of the downward-directed primary emission. This backscattered component can be significant, creating new features and/or distorting or masking features in the primary spectrum, and so substantially modifying key diagnostics such as the electron energy budget.

Photons of energy above ∼100 keV penetrate so deeply that they are lost to the observer, while below ∼10 keV they are mostly photoelectrically absorbed (e.g., Tomblin 1972). Therefore, the reflectivity of the photosphere has a broad hump in the range 10–100 keV, with a maximum around 30–40 keV. At some energies and view angles the reflectivity approaches 90%, so the observed spectrum may be very substantially affected by backscatter. This effect is well-known in solar physics and more generally in X-ray astronomy (see Magdziarz and Zdziarski 1995), and there have been several discussions of its influence on observed X-ray spectra (e.g., Tomblin 1972; Santangelo et al. 1973; Bai and Ramaty 1978), and on the electron spectra inferred from them (e.g., Johns and Lin 1992b; Alexander and Brown 2002; Kašparová et al. 2005; Kontar et al. 2006).

Understanding and modeling backscatter (albedo) has become even more important with the advent of high quality X-ray spectra from *RHESSI* (Lin et al. 2002) with spectral resolution as high as $\simeq 1$ keV, in combination with uncertainties as low as a few percent (for strong flares). Generally, contamination of the observed X-ray spectrum by reflected photons leads to a flattening of the spectrum and hence to an underestimation of the electron spectral index if the contribution of backscattered photons is not taken into account (Bai and Ramaty 1978). Extrapolation to low electron energies using such an underestimated spectral index leads to a substantial underestimation of the total electron energy in a flare. Indeed, a low-energy cutoff in an uncorrected electron spectrum is not even required if a "true" primary (albedo-corrected) electron spectrum can be used (Kontar et al. 2006).

3.1 Spectroscopy of the Photospheric Albedo

Downward-emitted photons are either absorbed or Compton-scattered, with some of the latter returned toward the observer, adding to the total flux detected (X-ray albedo). Scattering takes place on electrons, whether free or atomic. To account for elements heavier than hydrogen, the Compton cross-section is multiplied by an effective mean atomic number $Z = 1.2$ (e.g., Aschwanden 2005, for element abundances). The detailed density structure of the medium is irrelevant (Tomblin 1972).

Absorption, on the other hand, does depend strongly on chemical composition, and the best estimate of photospheric abundances should be included. The heavy elements Fe/Ni play the most important role from 6–8 keV up to ∼30 keV, while lighter elements contribute below 6 keV (Morrison and McCammon 1983).

3.1.1 Green's Function Approach

Propagation, absorption, and Compton scattering of primary hard X-rays can be straightforwardly studied using Monte-Carlo simulations (e.g., Bai and Ramaty 1978). This technique is ideal for obtaining the reflected, and hence the total observed, photon spectrum for a given form of the primary X-ray spectrum. However, the primary spectrum is generally unknown and unlikely to be an exact power-law, as is sometimes assumed. Therefore, an approach independent of the primary spectrum is required (Kontar et al. 2006).

For any isotropic primary spectrum $I_P(\epsilon_0)$ (photons cm^{-2} s^{-1} keV^{-1}) we can write the secondary, backscattered spectrum $I_S(\epsilon)$ as

$$I_S(\epsilon, \mu) = \int_{\epsilon}^{\infty} I_P(\epsilon_0) G(\mu, \epsilon, \epsilon_0) \, d\epsilon_0, \tag{3.1}$$

where $G(\mu, \epsilon, \epsilon_0)$ is an angle-dependent Green's function and $\mu = \cos\theta$, where θ is the heliocentric position angle of the primary hard X-ray source, or the angle between the Sun center—observer and Sun center—X-ray source lines. The observed spectrum, at photon energy ϵ and direction μ, is $I_S(\epsilon) + I_P(\epsilon)$. The importance of not averaging over viewing angle may be seen from Bai and Ramaty (1978). Using Green's function analytical fits to Monte Carlo simulations derived by Magdziarz and Zdziarski (1995), Kontar et al. (2006) calculated functions $G(\mu, \epsilon, \epsilon_0)$ shown in Fig. 3 for solar flare parameters. Green's functions, as calculated, account for Compton scattering and bound-free absorption.

The shape of the Green's function depends on the energy of the primary photon. For primary photons with low energies $\epsilon_0 < 30$ keV, the Green's function has a rather simple structure close to a Dirac delta-function (Fig. 3), showing that backscattering is dominated by the first scattering (especially at low energies), with the contributions from higher orders of scattering being generally small.

3.1.2 Reflected X-ray Photon Spectrum

Because the reflectivity is spectrum-dependent (Fig. 4), the albedo spectrum also depends on the shape of the primary spectrum (Kontar et al. 2006; Kotoku et al. 2007). While previous studies considered only the results for prescribed power-law or thermal primary spectra (cf. Bai and Ramaty 1978; Johns and Lin 1992b; Alexander and Brown 2002), the Green's function method allows more general forms of the primary spectrum.

Fig. 3 Green's functions $G(\mu, \epsilon, \epsilon_0)$ [keV^{-1}], including Compton scattering and photoelectric absorption, for three primary photon energies $\epsilon_0 = 20, 80, 300$ keV and $\mu = 0.7$ ($\theta \approx 45°$) calculated using approximations (Magdziarz and Zdziarski 1995) for solar conditions (after Kontar et al. 2006)
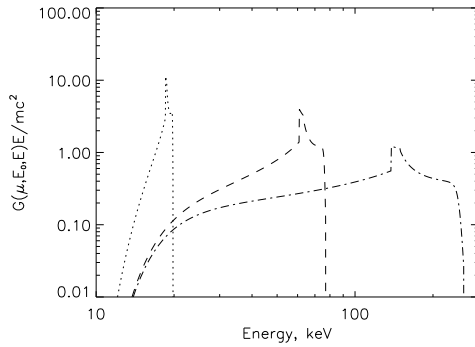
Fig. 4 *Upper panel:* Primary (*solid line*), reflected (*dotted line*) and total (*dashed line*) photon spectra calculated assuming a primary spectrum $I_P(\epsilon) \propto \epsilon^{-3}$, and using the Green's function for an X-ray source at heliocentric angle $\theta = 45°$. *Lower panel:* Reflectivity, defined as the ratio of reflected to primary fluxes $R(\epsilon, \theta = 45°) = I_R(\epsilon)/I_P(\epsilon)$. The reflectivity taken from Bai and Ramaty (1978) is shown with *diamonds*. Two absorption edges of Fe at 7.1 keV and Ni at 8.3 keV are seen in the reflected component (after Kontar et al. 2006)
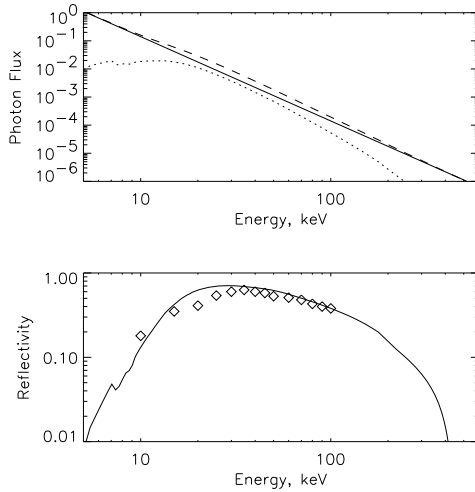
The total observed spectrum $I(\epsilon)$ is given by

$$I(\epsilon, \mu) = I_P(\epsilon) + \int_\epsilon^\infty I_P(\epsilon_0) G(\mu, \epsilon, \epsilon_0) \, d\epsilon_0. \qquad (3.2)$$

For a measured $I(\epsilon, \mu)$, we may obtain the primary spectrum $I_P(\epsilon)$ by solving the integral equation (3.2). In practice measurements yield discrete quantities and the integral equation (3.2) is used in the matrix form

$$I(\epsilon_i, \mu) = I_P(\epsilon_i) + G_{ij}(\mu) I_P(\epsilon_j), \qquad (3.3)$$

where we have used the summation convention for repeated indices, and introduced the *Green's matrix*

$$G_{ij}(\mu) = \int_{\epsilon_j}^{\epsilon_{j+1}} G(\mu, \epsilon_i, \epsilon_0) \, d\epsilon_0. \qquad (3.4)$$

Due to sharp features in the Green's function (Fig. 3), the integration in (3.4) is best performed via a change of variable to the wavelength (reciprocal energy) domain.
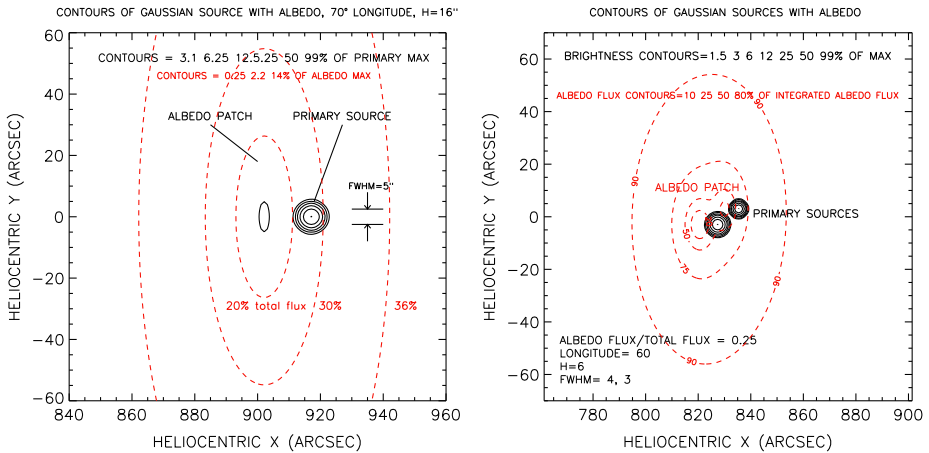
Fig. 5 *Left panel:* Model of a single primary source with albedo contours. The *solid contours* at logarith-mically-spaced intervals show the primary source down to 6.25% of the maximum, and the brightest portion of the albedo patch at 3.1% of the peak of the primary. The *dashed red contours* show the integrated flux of the albedo patch. Note that 50% of the albedo flux arises from an area about 10 times larger than the primary source, given its height of 12 Mm. *Right panel:* A model of a double source 10 Mm above the photosphere with the resultant albedo patch shown by flux contours (*red dashes*). There is considerable overlap of the primary source and albedo patch in this case (after Schmahl and Hurford 2002)

3.2 Imaging of Photospheric Albedo

3.2.1 Expected Spatial Signatures of Albedo

Before considering observational approaches to the spatial isolation of albedo, it is instructive to consider an elementary model of the solar backscattering process. To do this, we make four simplifying assumptions (e.g., Brown et al. 1975): first, that the primary bremsstrahlung is generated as a point source at a height h above a planar scattering surface; second, that this surface is perpendicular to the line of sight (e.g., disk center flare); third, that the primary X-ray emission and backscattering processes are isotropic; and fourth, that absorption of the scattered photons can be neglected. With such a scenario, the albedo source would extend out to the horizon as seen from the primary source. The albedo surface brightness would be determined by the distance from the primary source and the scattering location and by a cosine illumination factor and so the surface brightness would fall off as $(1 + [r/h]^2)^{-3/2}$, where r is the radial distance between the scattering location and the sub-source point on the scattering surface. Note that the scale of the radial profile is determined by the height of the primary source.

The implications of easing some of the restrictions in this simple model are illustrated in Fig. 5. For a primary source with finite size or structure, the resulting albedo patch would be a convolution of the primary source with the aforementioned profile. For a primary source located away from disk center, the center of the albedo patch is displaced toward disk center and presents an elliptical shape oriented parallel to the limb.

More rigorous calculation of the spatial properties of an albedo patch are provided by Bai and Ramaty (1978) who show, for example, that limb darkening would make the albedo more easily detected near disk center. In addition, the albedo patch will be energy- and primary-spectrum-dependent (Kontar and Jeffrey 2010). Nevertheless, the simplified model

does suggest that the albedo has three potentially observable spatial signatures: first, for sufficiently high primary source altitudes, the albedo would be significantly larger in extent than the primary source, with a size scale that increases with source height; second the albedo source would be displaced toward disk center by a distance $h \sin \theta_\odot$, where $\theta_\odot$ is the heliocentric angle; third, the albedo source would be elongated parallel to the limb with a minor to major axis ratio of $\cos \theta_\odot$. Observationally, however, because of the relative size scales of the primary source and its albedo patch, the albedo surface brightness would be only a small fraction (typically only a few percent) of that of the primary source. This would pose a potential challenge for conventional imaging systems because of scattered light; for reconstructed *RHESSI* hard X-ray images, typically limited in dynamic range to about 10:1, this would seem to make the spatial detection of albedo even more problematic.

3.2.2 The Spatial-Frequency Signature of Albedo

The potential observational difficulties posed by the low surface brightness of the albedo source can be eased if we Fourier transform the source of size $\sim d$ with the distribution $\exp(-x^2/d^2)$ and consider the amplitude of the Fourier components as a function of spatial frequency $\propto \exp(-k^2 d^2)$, where k is the spatial frequency. Compact primary sources have Fourier amplitudes that fall off at high spatial frequencies $kd \gg 1$. For spatial periods large compared to the source dimension $kd \ll 1$, however, the amplitudes are effectively constant. Further, the Fourier transform of the $(1 + [r/h]^2)^{-3/2}$ profile of an albedo source implies an amplitude that varies as e^{-kh}, where k is the spatial frequency. As illustrated in the lower half of Fig. 2 in Schmahl and Hurford (2002), this could be readily distinguished from that of the primary source. In effect. the Fourier transform integrates over the faint, distributed albedo source so that it becomes potentially detectable. The most obvious albedo signature would then be an "excess" in Fourier amplitude at low spatial frequencies over that expected for the compact primary source. The excess would be comparable to the reflected fraction, viz., up to several tenths (Bai and Ramaty 1978; Kontar et al. 2006). This is relevant to *RHESSI*, because with nine logarithmically-distributed spatial frequencies, its rotating modulation collimators (RMCs) directly measure the Fourier components of the source distribution.

3.2.3 Detection of a "Halo" Component

Applying such considerations to flare observations, early analysis of *RHESSI* data (Schmahl and Hurford 2002) directly fit the observed modulated light curves to derive an average modulation amplitude for each RMC. This technique, although simple, assumed circularly symmetric sources and was subject to potential statistical issues since it directly fit the counts which were only sparsely populating the short time bins. Nevertheless, the analysis showed (Fig. 6) that the modulation amplitude continued to increase toward the coarsest subcollimator even though the latter had a $183''$ spatial resolution (Hurford et al. 2002). This was taken as evidence of a hard X-ray "halo" component, consistent with expectations from albedo.

The analysis was refined by Schmahl and Hurford (2003), who formed individual back-projection images with the nine RMCs. In this case, the peak calibrated intensity of each back-projection image corresponded to the azimuthally-averaged modulation amplitude for the corresponding spatial frequency. The results, illustrated in Fig. 7, confirmed the presence of a non-Gaussian large-scale component consistent with a halo source. This technique alleviates potential statistical concerns associated with directly fitting the sparsely-populated time bins, but still requires circular sources for unambiguous interpretation.

FITS OF RELATIVE AMPS TO
log ρ = a k^b
Goodness of fit measured by
σ = RMS deviation.
b=1 implies powerlaw,
b=2 implies gaussian

FEB 20 09:58
σ=0.0373892
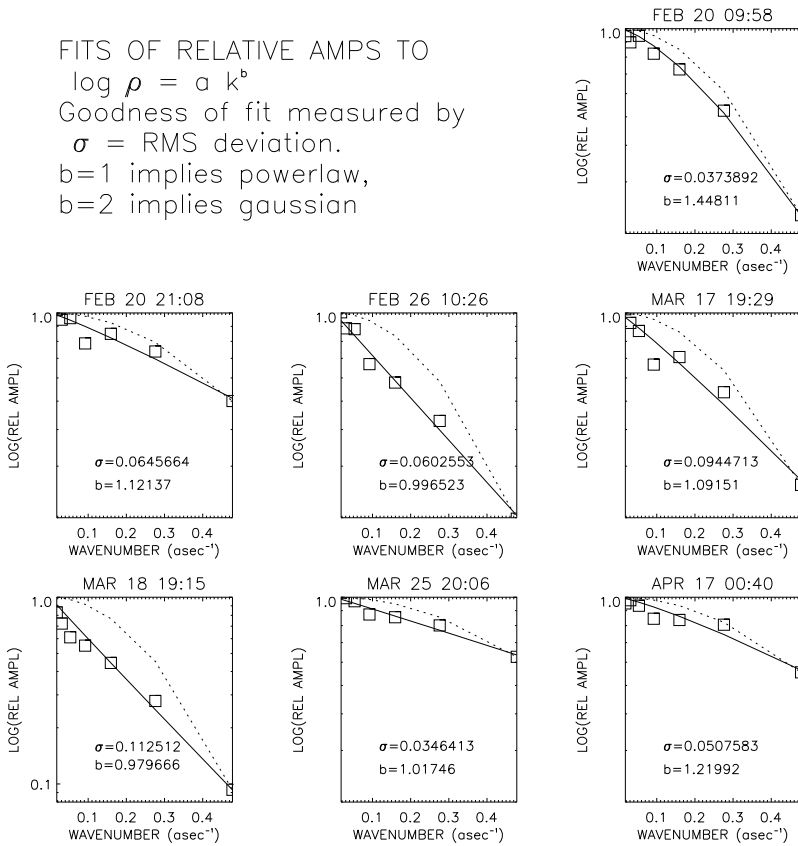b=1.44811

FEB 20 21:08
σ=0.0645664
b=1.12137

FEB 26 10:26
σ=0.0602553
b=0.996523

MAR 17 19:29
σ=0.0944713
b=1.09151

MAR 18 19:15
σ=0.112512
b=0.979666

MAR 25 20:06
σ=0.0346413
b=1.01746

APR 17 00:40
σ=0.0507583
b=1.21992

Fig. 6 Relative amplitudes of 7 flares vs. spatial frequency in the energy range 12–25 keV. The departures of the profiles from a Gaussian shape are interpreted as a "halo" component. Since (for computational simplicity) the fits were assumed to be azimuthally symmetric, the profiles must be considered to be polar averages over 360 degrees of rotation (after Schmahl and Hurford 2002)

3.2.4 Direct Use of Visibility Measurements

Since the initial reports of the halo component, analysis techniques have been developed that enable the *RHESSI* data to be directly transformed into calibrated measurements of the visibilities (specific Fourier components) as a function of spatial period and orientation (Schmahl and Hurford 2002; Schmahl et al. 2007). There are several reasons why visibilities are more appropriate for albedo determination: the visibilities are fully calibrated so that instrumental issues can be cleanly separated from solar issues; the expected visibilities can be directly calculated from source models; each visibility measurement is independent and has well-determined statistical errors whose propagation can guide subsequent conclusions; visibilities can be readily calculated using code that is now an integral part of the *RHESSI* object-oriented software package; visibilities are determined from linear transforms of the observed count rates, so that they can be combined in time or energy as desired; visibilities are well-suited to more complex sources since an observed visibility is the sum of the corresponding visibilities of its components.
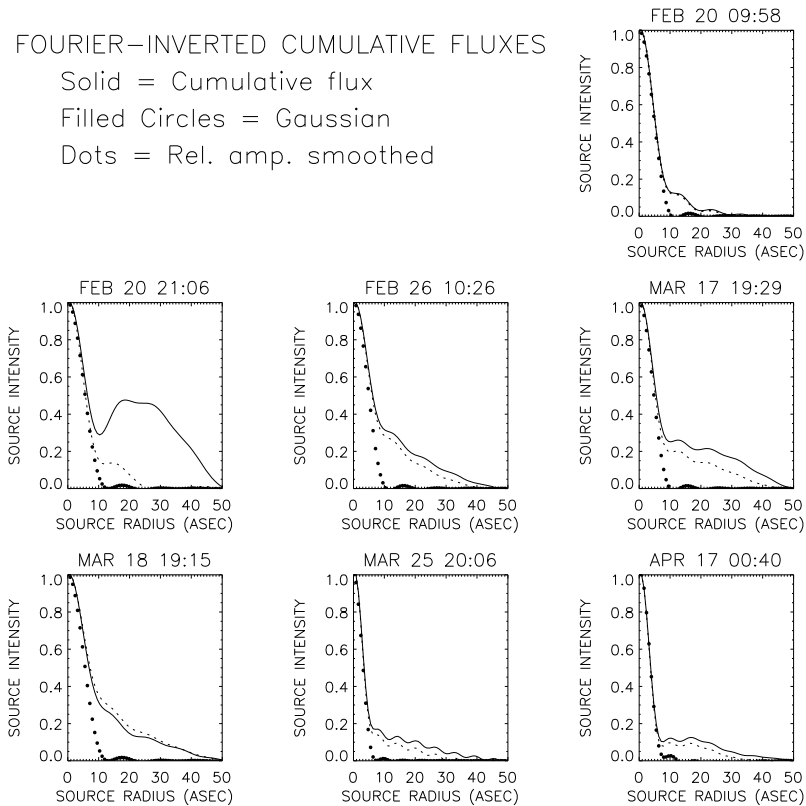
Fig. 7 A Fourier inversion produces the brightness profile in the energy range 12–25 keV. Since the albedo surface brightness is very low, the cumulative integrated flux from r to ∞ is plotted as a function of r. If the primary source profile is Gaussian, the integrated flux profile is Gaussian. The clear departures from a Gaussian shape in these profiles indicates the presence of extended sources inferred to be albedo patches (after Schmahl and Hurford 2003)

Figure 8 illustrates observations expressed in terms of visibilities. This event occurred at about 60° longitude, so the albedo emission is expected to be relatively weak, although there may be a signature of albedo for subcollimators 8 and 9, as indicated by the excess observed flux over the model flux.

3.2.5 Future Prospects for Visibility-Based Albedo Measurements with RHESSI

In the context of albedo, visibilities are used in two ways: first, to generate maps of the source using a direct visibility imaging method [such as back-projection (MEM-NJIT) (Schmahl et al. 2007) to obtain primary source positions and fluxes; and second, to use a visibility-based forward-fit algorithm to parameterize simple models of the primary source and the corresponding parameters of the albedo component (size, intensity, ellipticity, location) or maximum entropy.

The MEM-NJIT mapping algorithm is useful for obtaining the qualitative source configuration, although it is less reliable for quantitative measurement of source sizes. On the other hand the forward-fit algorithm requires a good starting point in parameter space, but can yield reliable source parameters.
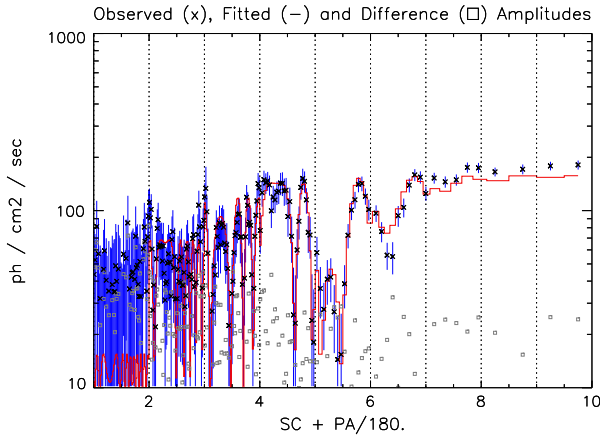
Fig. 8 Observed visibility amplitudes (*crosses* with *blue error bars*) for a flare interval as a function of subcollimator (SC = 1–9) and position angle (PA = 0–180°) of the grids in the energy range 12–25 keV. Each of the 9 *vertical panels* shows the amplitude as a function of PA for one subcollimator (labeled by *digits below the X-axis*). The *red curve* represents a model using two Gaussian sources, and the *squares* show the residuals relative to the model. For a given subcollimator (5 and 6 are good examples), the amplitude rises and falls while the grids rotate from PA = 0 to PA = 180°. Such patterns can correspond to an extended or double source

There are practical difficulties that remain to be overcome. As suggested by Fig. 8, the relative calibration (to within ∼5%) of the different subcollimators (especially the coarse ones) is critical to the isolation of albedo. Regrettably, the detector-to-detector calibration cannot currently support such an objective. However, using relative visibilities (viz., normalizing each RMC's visibilities to that detector's spatially integrated response) eliminates the effects of the detectors' relative efficiencies and so provides a potential approach to bypassing the calibration issue. Confirmation of this approach could be achieved with near-limb flares (presumed to be without significant albedo) or at energies where the albedo component is minimal. Other potential improvements are corrections for azimuthal averaging in each visibility, improvements in the present forward fit algorithm, perhaps with the use of an alternative search algorithm and with the use of third harmonic to add additional spatial frequencies visibilities.

The first flares for which albedo can be parameterized will necessarily be spatially simple (single, compact, and strong) and located within a few arc min of disk center. Eventually, it is expected that spectroscopic tools for albedo will be combined with imaging tools to provide comprehensive albedo information for a large subset of *RHESSI* flares. Since the albedo intensity and location depends on electron directivity, the potential reward of spatially-based albedo diagnostics is well worth the effort required to refine the analysis tools (Kontar and Brown 2006b).

4 The Electron Energy Spectrum

In this section, the angular dependence of the bremsstrahlung cross-section and the angular/spatial/temporal characteristics of the electron distribution are neglected. The primary source photon spectrum $I_P(\epsilon)$ may be therefore treated simply as the convolution in electron energy of the solid-angle-averaged bremsstrahlung cross-section and the mean source electron flux (2.4).

In general, we first correct for instrumental effects (see Smith et al. 2002; Schwartz et al. 2002) such as pulse pileup,[3] then correct the observed hard X-ray spectrum for albedo effects (Sect. 3.1) to obtain the primary source spectrum $I_P(\epsilon)$. As explained in Sect. 2, the functional form of the primary photon energy spectrum $I(\epsilon)$ (subscript 'P' hereafter understood) contains crucial information on the form of the *mean source electron flux spectrum* $\overline{F}(E)$, information that may in turn be used to reveal properties of the electron acceleration and propagation processes.

We first discuss forward fitting (Sect. 4.1) and regularized inversion (Sect. 4.2) methods of extracting the electron energy spectrum $\overline{F}(E)$ from noisy hard X-ray data $I(\epsilon)$.

4.1 Forward Fitting

Forward fitting is the process of quantitatively comparing a parameterized model with observational data. Criteria are established to determine acceptable fits and, if the model is capable of providing acceptable fits, a best fit, that gives the most probable values of the model parameters, is determined by minimizing chi-squared (χ^2), the sum of the squares of the normalized residuals.[4]

Models may be based on the apparent structure of the data, a physical model, or a combination of the two. At the lowest X-ray energies, *RHESSI* flare spectra can contain *thermal bremsstrahlung* and *free-bound* (recombination) continua from the hottest plasma in flares, in addition to spectral lines (e.g., Phillips et al. 2006). The X-rays at higher energies (normally $\gtrsim$10–20 keV) are dominated by electron-ion bremsstrahlung from energetic, nonthermal electrons (Sect. 2.1). Free-bound radiation from nonthermal electrons may also contribute (Sect. 2.2). At higher energies, electron-electron bremsstrahlung can become significant (Sect. 2.3). At γ-ray energies, spectral lines excited by energetic, nonthermal ions and positronium continuum emission can be present. The quality of a fit is also dependent on a careful subtraction of background counts before obtaining the spectral fit. Spectral fits are only reliable over the range of photon energies for which the flare emission is well above the background.

RHESSI's high spectral resolution often makes it easy to distinguish the thermal component of an X-ray spectrum from the nonthermal component, especially in large flares. An example of this is shown in the top panel of Fig. 9, a spatially-integrated spectrum from SOL2002-07-23T00:35 (X4.8); below a photon energy ∼40 keV, the thermal component clearly dominates over the flatter nonthermal component. For many spectra, however, the thermal and nonthermal components are not so clearly distinguishable. This was the case during the early rise of SOL2002-07-23T00:35 (X4.8), for example (Holman et al. 2003). For these spectra, the most likely model can sometimes be deduced from the time evolution of the flare spectra and/or flare images (cf. Sui et al. 2005).

The thermal component of the spectrum can typically be well fitted with the form of $I(\epsilon)$ from an isothermal plasma at temperature $T : I(\epsilon) \propto (EM/\epsilon T^{1/2}) \exp(-\epsilon/kT)$, where k is

---

[3]Pulse pileup is an issue for large solar flare spectra with high count rate in *RHESSI* detectors. Un-physical counts are recorded when pairs (or more) of low-energy photons, arriving nearly simultaneously, are detected as a single energy count at higher energies (for details, see Datlowe 1976b, 1976a). Current pileup corrections for spatially integrated spectra have limited precision that might be inadequate for the events with extremely high count rates. As of April 2011, no standard image pileup corrections yet exist.

[4]A normalized residual is defined as the difference between the measured and model-predicted value, divided by the uncertainty in the measured value. The division by the uncertainty gives greater weight to measured values with smaller relative uncertainties (e.g., Chap. 15 of Press et al. 1992).

Fig. 9 Fit to a
spatially-integrated spectrum
from SOL2002-07-23T00:35
(X4.8). *Top panel:* Photon flux
spectrum (*plus signs*) integrated
over the 20 s time period
00:30:00–00:30:20 UT. A fit to
the spectrum (*solid curve*)
consisting of the sum of the
bremsstrahlung from an
isothermal plasma (*dotted curve*)
and the bremsstrahlung from a
double power-law mean electron
flux distribution with a
low-energy cutoff. *Middle panel:*
Residuals from the fit in the *top
panel* (observed flux minus
model flux divided by the 1σ
uncertainty in the observed flux).
Bottom panel: Best fit mean
electron flux distribution times
the mean plasma density and
source volume, plotted as a
function of electron energy in
keV (after Holman et al. 2003).
Note that pulse pileup (Smith et
al. 2002;
Kontar et al. 2003) might be an
issue for this flare
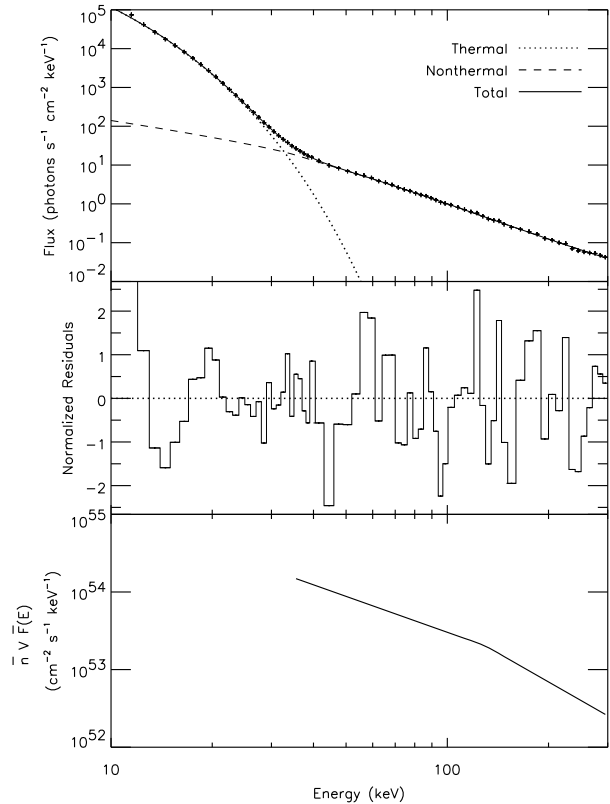
Boltzmann's constant and EM is the emission measure ($\int n_e n_i \, dV$). The fit in Fig. 9, for example, gave a temperature of 37 MK and an emission measure of 4.1×10^{49} cm^{-3}. A fit to thermal bremsstrahlung alone is often adequate, but this does not account for the spectral line complexes at ~6.7 keV and ~8 keV or for recombination radiation.[5] The thermal component of *RHESSI* spectra is now routinely fitted (included into standard *RHESSI* software) using the latest version of Chianti (Landi et al. 2006), which incorporates all the emission mechanisms important at low energies. The multithermality of plasma and the corresponding emission measure differential in temperature are addressed in Sect. 4.6.

The nonthermal component of the spectra can usually be fitted adequately with either a single or a double power-law photon flux spectral model. Sometimes a third, flatter power-law component is included at low energies to simulate a low-energy cutoff in the electron distribution. Such fits are useful for examining the evolution of flare spectra with time. They do **not**, however, contain any direct physical information about the electrons responsible for the observed emission. It is therefore more interesting to fit the photon spectra with the radiation from a model *electron* distribution, typically assumed to have the form of a double power law with a possible low- and/or high-energy cutoff. This form allows sharp breaks in

---

[5]RHESSI spectroscopy in the range of energies below ~10 keV is often complicated by non-diagonal instrument response (Smith et al. 2002; Schwartz et al. 2002) and some instrumental features (Phillips et al. 2006).
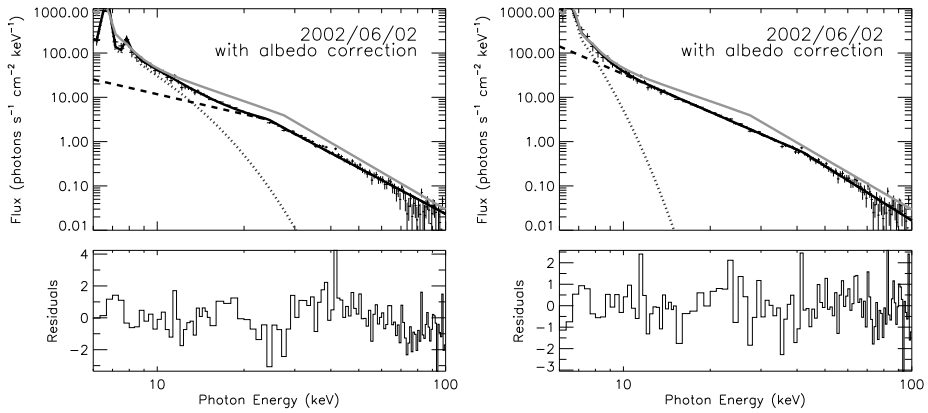
Fig. 10 Albedo-corrected *RHESSI* spectrum (*crosses* with *error bars*) at the hard X-ray peak (11:44:28–11:44:32 UT) of SOL2002-06-02T20:44 (M1.0). The *solid line* shows the combined isothermal (*dotted line*) plus double power-law (*dashed line*) spectral fit. The spectral fit before albedo correction is over-laid (*gray, solid line*). *Left panel:* The nonthermal part of the spectrum is fitted to a double power-law model with a break energy at ∼21 keV. *Right panel:* The same spectrum is fitted to a double power-law model with a break energy at ∼40 keV. The reduced χ^2 values of the fits in the *left and right panels* are 1.4 and 1.0, respectively. The normalized residuals are plotted below each spectrum (after Sui et al. 2007)

the electron distribution (either a mean electron flux $\overline{F}(E)$; Equation (2.4) or, for a thick-target model, an injected electron distribution $\mathcal{F}_0(E_0)$; Equation (2.7)). However, due to the filtering of the bremsstrahlung cross-section $Q(\epsilon, E)$, such breaks are generally smoothed out in the corresponding photon spectrum $I(\epsilon)$.

The nonthermal part of the flare spectrum in Fig. 9 is fit with the bremsstrahlung from a double power-law mean electron flux distribution with a low-energy cutoff

$$\overline{F}(E) = \begin{cases} 0; & E < E_c \\ AE^{-\delta_1}; & E_c < E < E_b \\ AE_b^{\delta_2-\delta_1}E^{-\delta_2}; & E_b < E \end{cases} \qquad (4.1)$$

(bottom panel). The highest value of the low-energy cutoff E_c consistent with a good fit to the data was used; the value of E_c is not constrained below this value because of the dominance of thermal radiation. This fit therefore provides a lower limit to the energy in nonthermal electrons. The spectrum could not be acceptably fit with a single power law; note that the location of the break energy E_b is at a higher energy than the apparent location of the break in the photon spectrum; this is because all electrons with energies above a given photon energy contribute to the radiation at that photon energy.

The photon spectrum residuals (using a sum of the isothermal and nonthermal models) are shown in the middle panel of Fig. 9. Besides providing a reduced χ^2 (χ^2 divided by the number of degrees of freedom in the fit) close to 1, the residuals from a good fit should be random and uncorrelated and have a near-normal distribution $N(0, 1)$. For the event in question, the residuals do *not* exhibit this desired behavior, with significant deviation at photon energies between 10 and 15 keV (see Caspi and Lin 2010). Practically, a broad spectral "line" is often included in the model to account for this feature; with the inclusion of this ad hoc feature, it is generally possible above ∼10 keV to obtain good fits to the *RHESSI* spectra without assuming the presence of any systematic uncertainty in the data above the level of Poisson noise.

A comparison of a poor forward fit (left panels) to a good forward fit (right panels) is shown in Fig. 10. Both fits are to the same spectrum and in both the model is bremsstrahlung from an isothermal plasma plus a double power-law photon spectrum. In the fit on the left, the break energy E_b is fixed at a value $\sim$21 keV, so the model is a single power law above this energy. In the fit on the right, the break energy is allowed to adjust to a value that gives the best fit to the data. The reduced χ^2 for the fit on the right is 1.0; in the fit on the left it is 1.4, still consistent with an "acceptable" fit. However, the "long wavelength" oscillation in the residuals for the fit on the left provides the most obvious clue that the model is *not* adequate; the overall shape of the spectrum is not consistent with the assumed model form. Adding more parameters (in this case a variable break energy E_b) results in a more acceptable distribution of residuals, as in the right panel (Fig. 10).

The gray curves in Fig. 10 are fits to the data before albedo, assumed to be from isotropically-emitted photons, is taken into account (see Sect. 3.1). They demonstrate the significant impact that albedo can have on the inferred spectrum of the emitted radiation.

An inadequately resolved issue with forward fitting is determining the uncertainty in the fit parameters and the resulting model function. Since, in general, the fit is not linear, the fit parameters are not independent and the uncertainties are not necessarily even symmetric around the best-fit values. In Fig. 10, for example, notice that the temperature of the isothermal component is adjusted to a higher value to compensate for the low break energy in the double power-law component (Sui et al. 2007). The uncertainty in the value of the low-energy cutoff to the mean electron flux fit function in Fig. 9 is small in the positive (higher-energy) direction, but indefinitely large in the negative direction! As long as a good initial choice is made for the fit parameters, the process of obtaining the best fits is relatively quick. An efficient method for determining the uncertainties in the fit parameters and function is not in place, however. Bayesian Monte Carlo approaches to determining these uncertainties are robust but slow. A practical solution to this important issue is badly needed.

4.2 Regularized Inversion

The unprecedented energy resolution of *RHESSI* hard X-ray spectra has introduced the need, perhaps for the first time in solar hard X-ray spectroscopy, to apply sophisticated mathematical tools for information retrieval in order to fully exploit the physical significance of the recorded spectra. It is well established that the most effective mathematical framework for this problem lies in the theory of linear inverse problems (e.g., Craig and Brown 1986). In this setting, linear integral equations of the first kind relate the photon spectrum ("data") to the electron spectrum ("source function"). Such equations are usually ill-posed in the sense of Hadamard—the effects of the experimental noise can be strongly amplified by the intrinsic numerical instability of the model (for details, see Bertero et al. 1985).

Standard approaches to obtain a solutions of inverse problem in solar X-ray spectroscopy are based on forward-fitting (e.g., Holman et al. 2003) the photon flux spectrum with parametric forms of the electron flux spectrum (see Sect. 4.1). However, in forward-fitting, the number of parameters utilized in the input form is generally small. This imposes severe, possibly artificial, constraints on the allowable form for the source function and is the main reason why inversion techniques (e.g., Bertero et al. 1985; Piana 1994), which find the best model-free non-parametric fit to the data subject to physically sound constraints, are currently a very promising approach to data analysis in solar hard X-ray spectroscopy.

A particularly promising technique is that of regularized inversion (e.g., Bertero et al. 1985). The essence of the regularization technique is to seek a least-squares solution of the

pertinent integral equation (e.g., (2.4)) within a subset of the solution space which accounts for some measure of a priori information on the source function. Consider the linear system

$$\mathbf{g} = \mathbf{A}\mathbf{f}, \tag{4.2}$$

which represents a discretized version of the (Volterra) integral equation (2.4), where

$$A_{ij} = \frac{1}{4\pi R^2} Q\left(\frac{\epsilon_i + \epsilon_{i+1}}{2}, \frac{E_j + E_{j+1}}{2}\right)\delta E_j, \quad i = 1, \ldots, N; \ j = 1, \ldots, M; \tag{4.3}$$

$\mathbf{f}$ is the "source vector" $\overline{n}V(\overline{F}(E_1), \ldots, \overline{F}(E_M))$, $\mathbf{g}$ is the "data vector" $(g(\epsilon_1), \ldots, g(\epsilon_N))$ (with $M \geq N$), and the $\delta\epsilon_i$ and δE_j are appropriate weights. The values $g(\epsilon_i)$ correspond to a set of discrete photon counts in energy bands $\epsilon_i \to \epsilon_i + \delta\epsilon_i$, while the $\overline{F}(E_j)$ are the corresponding values of the mean electron flux in energy bands $E_j \to E_j + \delta E_j$. Owing to the strong smoothing properties of the integral operators, the matrix $\mathbf{A}$ is quasi-singular and standard inversion routines cannot be effectively applied. However, Tikhonov regularization theory (Tikhonov 1963) obtains sufficiently smooth source functions as the (unique) solution of the minimization problem

$$\|\mathbf{g} - \mathbf{A}\mathbf{f}\|^2 + \lambda\|\mathbf{C}\mathbf{f}\|^2 = \text{minimum}, \tag{4.4}$$

where λ is the *regularization parameter*, which tunes the trade-off between the fitting term $\|\mathbf{g} - \mathbf{A}\mathbf{f}\|^2$ and the penalty term $\|\mathbf{C}\mathbf{f}\|^2$. If $\mathbf{C} = \mathbf{I}$, the method is termed *zero-order regularization* (Piana et al. 2003), while if $\mathbf{C}$ is the matrix corresponding to numerical differentiation, the method is termed *first-order regularization* (Kontar et al. 2004). The optimal choice of the parameter λ can be accomplished by means of some optimization approach or by means of a semi-heuristic technique based on a statistical analysis of the cumulative residuals (Piana et al. 2003).

The main disadvantage of using Tikhonov regularization is that for noisy data, solutions with negative (unphysical) values might result. A possible solution to this is provided by the projected Landweber method (Piana and Bertero 1997)

$$\mathbf{f}_{n+1} = P_+[\mathbf{f}_n + \tau\mathbf{A}^T(\mathbf{g} - \mathbf{A}\mathbf{f}_n)], \qquad \mathbf{f}_0 = 0, \tag{4.5}$$

where P_+ sets to zero all negative components at each iteration and τ is a relaxation parameter. In this framework, the tuning between stability and fitting is realized by applying some optimal stopping rule to the iterative procedure.

4.2.1 Validation of Regularization Techniques

The effectiveness of different inversion algorithms, including a standard forward-fitting technique, have been tested by Brown et al. (2006) using synthetic data. In this test six forms of the mean source electron spectrum $\overline{F}(E)$ in Fig. 11 (bottom), each one characterized by specific features like bumps or cutoffs, were used to generate the corresponding hard X-ray spectra $I(\epsilon)$ in Fig. 11 (top), and a realistic amount of Poisson noise added. In all cases, the photon spectra look smooth and quite similar in their shape, while the corresponding mean electron spectra exhibit very irregular behavior that is filtered out by the smoothing effect of the bremsstrahlung cross-section. These differences epitomize the mathematical concept of ill-posedness.

The comparisons used four different techniques: zero-order (Piana 1994) and first-order (Kontar et al. 2004) Tikhonov regularization, triangular matrix row elimination with variable
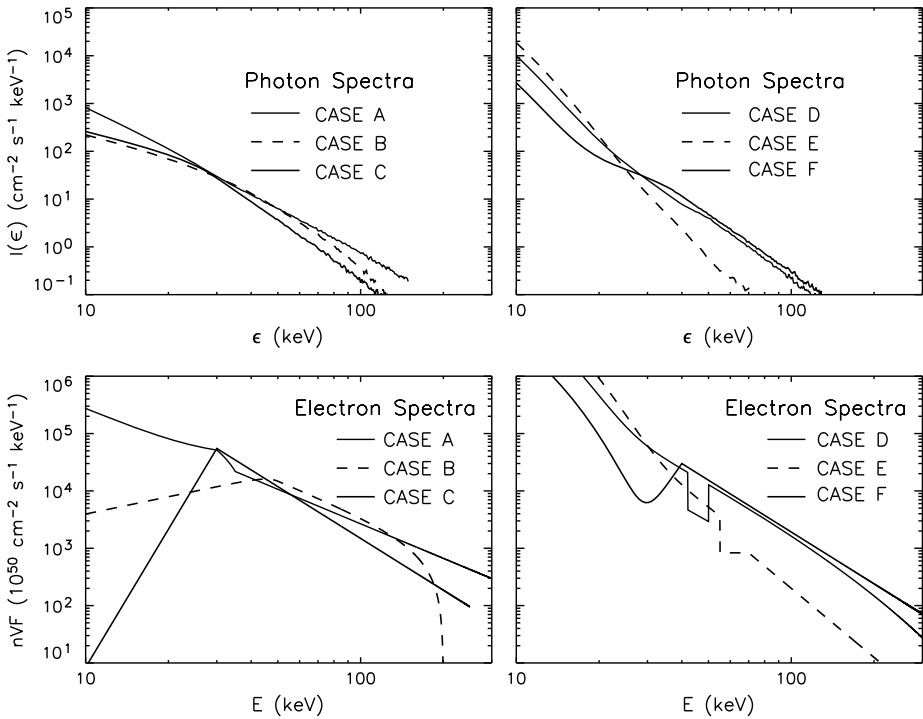
Fig. 11 Synthetic mean source electron spectra (*bottom*) and the corresponding photon spectra (*top*) in a "blind" experiment for assessing the effectiveness of different reconstruction methods in *RHESSI* X-ray spectroscopy (after Brown et al. 2006)

energy binning (Johns and Lin 1992b) and forward-fitting with a parametric form consisting of a double power law with low- and high-energy cutoffs plus an isothermal component (e.g., Holman et al. 2003). These tests were done "in the blind" to recover $\overline{F}(E)$ for later comparison with the true forms (Brown et al. 2006). All of these approaches were able to reconstruct the general magnitude and form of $\overline{F}(E)$, although forward-fitting inevitably fails to recover small features which are not coded within the parameterized form of the model function.

4.2.2 Application to RHESSI Data

The Tikhonov regularization method has been applied to hard X-ray measurements recorded by *RHESSI* for SOL2002-02-20T11:07 (C7.5), SOL2002-03-17T19:31 (M4.0), SOL2002-08-06T12:59 (C7.9) (Massone et al. 2003), SOL2002-02-26T10:27 (C9.6) (Kontar et al. 2005) and SOL2002-07-23T00:35 (X4.8) (Piana et al. 2003). In this last paper a "dip-hump" feature in the recovered mean source electron spectrum $\overline{n}V\overline{F}$ was noted near $E = 55$ keV (Fig. 12); such a feature is (by construction) absent in the superimposed forward-fit spectrum (Holman et al. 2003) using the same (Haug 1997) bremsstrahlung cross-section.

The 3σ error bars plotted in Fig. 12 clearly show that this "dip-hump" feature is statistically significant. Its physical interpretation is still an open issue, but it may reflect the depletion of low-energy nonthermal electrons due to the effect of Coulomb collisions for an injected distribution with a low-energy cutoff (Emslie and Smith 1984). On the other hand,
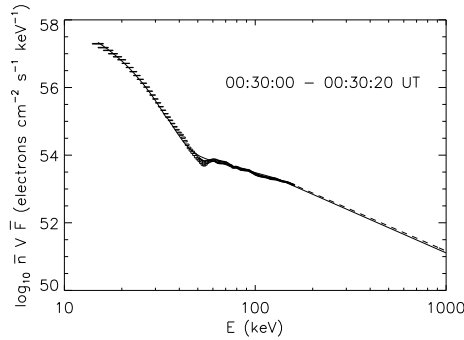
Fig. 12 Regularized spectrum $\overline{n}V\overline{F}$ versus electron energy E for the time interval shown in SOL2002-07-23T00:35 (X4.8). The spectrum has been extended at high energies using a power law of index $\delta = 2.45$ (*dashed lined*). The vertical size of the *error boxes* reflects the 3σ limit caused by statistical noise in the observed $I(\epsilon)$. The spectrum obtained by a forward-fitting procedure using the same bremsstrahlung cross-section is shown as a *solid line* (after Piana et al. 2003)

it may simply reflect an inadequate correction for the pulse pileup effect in the *RHESSI* detectors, with a resultant aliasing of the photon spectrum used in the construction of Fig. 12 (Smith et al. 2002; Kontar et al. 2003).

4.3 High-Energy Cutoffs in the Electron Distribution

It should be noted that the matrix **A** in (4.2) need not be square, so that the energy range corresponding to the electron flux (source) vector **f** may extend over a larger range than the photon flux (data) vector **g**. Physically, this corresponds to the production (through free-free bremsstrahlung only) of photons of energy ϵ by electrons of energy $E > \epsilon_{max}$, where ϵ_{max} is the largest photon energy observed. It should be noted that, because the bremsstrahlung cross-section $Q(\epsilon, E)$ is a non-diagonal matrix of E, the form of the photon spectrum at photon energy ϵ does provide information on the electron spectrum for all energies $E > \epsilon$, including those with $E > \epsilon_{max}$. Consequently, a distinct advantage of the regularization methodologies (over, say, the more straightforward matrix inversion method of Johns and Lin 1992b) is that some information can be obtained on the form of the electron spectrum $F(E)$ at energies beyond the maximum photon energy observed.

A particular example of this is the possible existence of a high-energy cutoff E_{max} in the *electron* spectrum $\overline{F}(E)$. Although for free-free emission this would correspond to a maximum photon energy $\epsilon_{max} = E_{max}$, ϵ_{max} may lie beyond the range of statistically useful photon (or count) data. However, as shown by Kontar et al. (2004), the regularized inversion method can, in principle, detect the presence of the high-energy cutoff at $E = E_{max}$ through its effect on the photon spectrum at observable energies ϵ that are all significantly less than E_{max}, and this technique was indeed used to discern a high-energy cutoff (or at least a very sharp downward spectral break) in the flare of SOL2002-02-26T10:27 (C9.6) by Kontar et al. (2005). The ability of the regularization technique to detect such high-energy cutoffs in the electron spectrum was dramatically highlighted in the validation study of Brown et al. (2006). In that study, a synthetic electron spectrum $\overline{F}(E)$ with a high-energy cutoff at 200 keV (case B in Fig. 11) was used to generate noisy photon "data" in the range wholly below 100 keV. Analysis of these "data" using both zero-order and higher-order regularization techniques rather faithfully reproduced the high-energy cutoff in the electron spectrum, with an accuracy better than 30%. High-energy cutoffs have
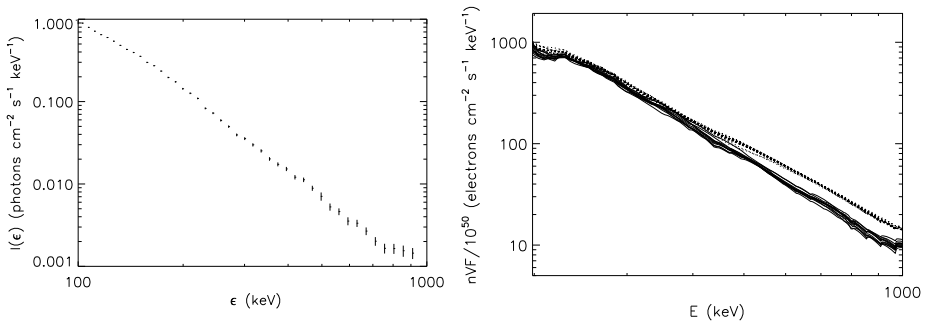
Fig. 13 *Left panel:* Photon spectrum for the time interval 09:43:16–09:44:24 UT in SOL2005-01-17T09:52 (X3.8), with gamma-ray lines removed. *Right panel:* Recovered forms of the quantity $\bar{n}V\overline{F}(E)$ (in units of 10^{50} electrons cm^{-2} s^{-1} keV^{-1}; see (2.4)) using a zero-order regularization technique and presented as a "confidence strip," i.e., a series of solutions, each based on a realization of the data consistent with the size of the uncertainties. The *dashed lines* assume electron-ion emission only; the *solid lines* include the additional electron-electron emission term (after Kontar et al. 2007)

had very limited use to date as a parameter in forward-fitting methods (Sui et al. 2002; Holman et al. 2003), although both forward-fit and direct matrix inversion methods (Johns and Lin 1992b) should be able to say something about the electron spectrum above maximum photon "data" energy, in that if there is a high energy cutoff E_{max} close to the maximum observed photon energy the spectral shape is much different.

4.4 Spectral Breaks in the Electron Distribution

Figure 13 shows the photon spectrum for the time interval 09:43:16–09:44:24 UT (the time of approximate peak flux) for SOL2005-01-17T09:52 (X3.8) (after Kontar et al. 2007). This event, which produced several strong gamma-ray lines, was previously studied by Kontar and Brown (2006b), who concluded that the pitch-angle distribution for electrons up to ∼300 keV was close to isotropic. There is evidence for an upward break in the spectrum at energies ≳300 keV. For completeness, we note that the energy range ≳300 keV also contains some pseudo-continuum γ-ray contributions from ions (e.g. Smith et al. 2003).

The mean source electron spectrum $\overline{F}(E)$ recovered from the photon data, using two different bremsstrahlung cross-sections—electron-ion only and (electron-ion + electron-electron) is shown in Fig. 13. (The results are presented in the form of two "confidence strips," bundles of solutions using different noisy realizations of the same data.) The $\overline{F}(E)$ recovered using the full cross-section (2.11), including electron-electron bremsstrahlung, is, for $E \gtrsim 300$ keV, steeper (spectral index greater by ∼0.4) than the $\overline{F}(E)$ recovered assuming purely electron-ion emission. Kontar et al. (2007) point out that while the upward break at $\epsilon \approx 300$ keV in Fig. 13 is real, the break at $E \simeq 400$ keV in the $\overline{F}(E)$ recovered using the electron-ion bremsstrahlung cross-section alone (Fig. 13) is an artifact of the neglect of electron-electron emission at energies ≳300 keV. The true form of $\overline{F}(E)$, obtained using the full cross-section, has a rather straightforward power-law form over the energy range from 200–1000 keV. As pointed out by Kontar et al. (2007), the inclusion of electron-electron bremsstrahlung may remove the need to explain "break energies" in several events (cf. Dennis 1985; Heristchi 1986; Li 1995; Trottet et al. 1998; Vestrand 1988). However electron-electron bremsstrahlung cannot explain spectral breaks at low energies ≤300 keV often observed in *RHESSI* spectra (e.g., Conway et al. 2003).

4.5 Low-Energy Cutoffs in the Electron Distribution

Given that nonthermal electron spectra often have a form close to a steep power law $E^{-\delta}$, with $\delta > 2$ (Dennis 1985), an accurate value for the low-energy cutoff E_c parameter is required to obtain values of the total energy in nonthermal electrons (see, however, Emslie 2003; Hannah et al. 2009). Thus, the determination of E_c plays a key role in the interpretation of hard X-ray data (see also Holman et al. 2011, this issue).

In most cases, the value of E_c must be somehow disentangled from the combined (thermal + nonthermal) form of $\overline{F}(E)$, and the value of E_c is, in general, only weakly constrained by observations. Some flares require rather high values of E_c to explain observations. The presence of a low-energy cutoff introduces a flattening of the photon spectrum at energies below E_c (see, e.g., Holman 2003; Huang 2009; Han et al. 2009). Nitta et al. (1990) show that the spectrum of the impulsive component flattens toward low energies, suggesting a value of E_c as high as 50 keV. Fárník et al. (1997), using *Yohkoh* data, observed a few flares with flat spectra below 30 keV.

Studies before *RHESSI* mostly assumed an arbitrary, fixed, value of E_c. More recently, using *RHESSI* high-spectral-resolution data (without albedo correction), several studies have reported clear evidence for a low-energy cutoff or even a dip (or gap) (e.g., Kontar and Brown 2006a) in the mean electron flux distribution $\overline{F}(E)$ between its thermal and nonthermal components, leading to a clear identification of a low-energy cutoff for the nonthermal electron distribution (Fig. 14).

Forward-fitting methods (Sect. 4.1) usually assume a strict low-energy cutoff, i.e., a sharp change in the $\overline{F}(E)$. However, as showed by, e.g., Kucera et al. (1996) or Kašparová et al. (2005), it is often not possible to determine a unique best spectral fit; fit parameters can be varied substantially without unacceptably large changes in the photon spectrum, with other free parameters compensating. In particular, because of the dominance of thermal emission at low energies, forward-fit approaches can reliably infer only *upper limits* to the value of E_c; values of E_c well below such upper limits provide equally good fits to an observed X-ray spectrum, with a somewhat different value of the thermal source temperature T. Moreover, as mentioned in Sect. 4.1 determining confidence intervals for model parameters is an extremely time-consuming task.

On the other hand, regularized inversion methods (Sect. 4.2) have proven their ability to detect dips in $\overline{F}(E)$ (see Piana et al. 2003). These methods also provide estimates of uncertainties in the solution, through so-called *confidence strips* in which 99% of data-consistent solutions lie; see Brown et al. (2006). Using this approach, clear low-energy cutoffs or dips in the mean electron flux distribution $\overline{F}(E)$ at an energy around 20–40 keV were reported by Kašparová et al. (2005) for SOL2002-08-20T08:25 (M3.4). Forward-fit methods yielded $E_c = 44 \pm 6$ keV, a somewhat higher value. Kontar and Brown (2006a) found a clear dip around 20 keV for the SOL2002-09-17T05:54 (C2.0) event. For further examples of low-energy cutoffs obtained through both forward-fitting and regularization, see Figs. 14 and 15, respectively.

Some flares, such as SOL2002-04-25T06:02 (C2.5), SOL2002-09-17T05:54 (C2.0), or SOL2002-08-20T08:25 (M3.4), have quite hard (flat) spectra with a relatively weak thermal components. Such a flat form of the photon spectrum can require (Kontar and Brown 2006a) a low-energy cutoff, or local minimum, in the corresponding mean electron distribution $\overline{F}(E)$. These local minima are particularly interesting, since if $\overline{F}(E)$ is sufficiently steep (steeper than E^1; see the remarks after (2.9)), it could have a form inconsistent with the widely-used collision-dominated thick-target model for X-ray production (Kontar and Brown 2006a; Brown et al. 2009).

Fig. 14 Mean electron flux spectra $\overline{n}V\overline{F}(E)$ of SOL2002-09-17T05:54 (C2.0) recovered using forward fitting. The *solid/dashed lines* show the spectrum without/with the albedo correction (after Kontar et al. 2006)
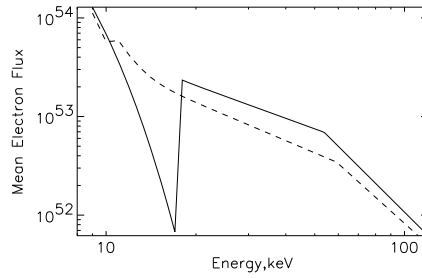

Fig. 15 Mean source electron flux spectrum $\overline{n}V\overline{F}(E)$ for SOL2002-08-20T08:25 (M3.4) for the time interval 08:25:20–08:25:40 UT recovered using regularized inversion. The *solid line* shows the spectrum without albedo correction. The confidence intervals represent the range of solutions found for different statistical realizations of the photon spectrum (after Kontar et al. 2006)
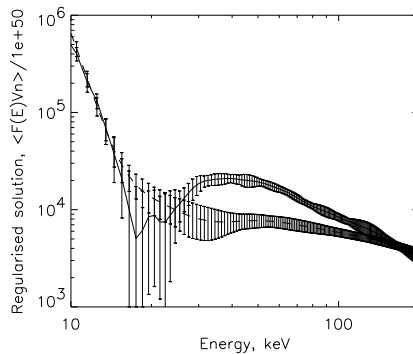
However, the effects of Compton backscattering (Sect. 3.1) on the hard X-ray spectrum are most pronounced for flares with such hard spectra. Kašparová et al. (2007) showed that the flares listed above are all located close to solar disk center ($\mu > 0.5$, $\theta < 60°$; denoted as stars in Fig. 18) and they therefore attributed the flat spectra to the heliospheric-angle-dependent albedo (Sect. 3.1). This result is consistent with earlier observations of Nitta et al. (1990) and Fárník et al. (1997), who observed several flares with flat spectra which were located not far from disk center ($\mu \geq 0.6$) or from near center ($\mu \approx 1.0$), respectively. Interestingly, adding considerations of the albedo in such events (Kontar et al. 2006) removes the spectral hardening, and hence the need for a low-energy cutoff in this photon energy range—see Figs. 14 and 15, Kašparová et al. (2005), and Kontar et al. (2006). Recently, Kontar et al. (2008a) have analyzed a large number of solar flares with weak thermal components and flat photon spectra. It has been shown that if the isotropic albedo correction is applied, all low-energy cutoffs in the mean electron spectrum are removed, and hence the low-energy cutoffs in the mean electron spectrum of solar flares above ∼12 keV cannot be viewed as real features. If low-energy cutoffs exist in the mean electron spectra, their energies should be less than ∼12 keV. Thus, the apparent low-energy cutoff in the mean electron distribution is most likely to be a feature connected with albedo; it is *not* a true physical property (Hannah et al. 2009). This result can substantially change the total electron energy requirements in a given flare.

In summary, our view on the existence and/or value of low-energy cutoffs has been significantly broadened since high quality *RHESSI* observations have become available. Yet, the determination and even the existence of a low-energy cutoff remains a very complex issue. First, the contribution of the photospheric albedo to the observed photon spectrum must be taken into account and removed before the observed photon spectrum is converted to the electron distribution. Such correction removes apparent energy cutoffs in the mean electron distribution above ∼12 keV (Kontar et al. 2008a). Secondly, apparent evidence from

hard X-ray emission for a low-energy cutoff in the electron spectrum should be carefully combined with other data sensitive to the low-energy cutoff in nonthermal electron distribution, e.g., microwave spectra (Holman 2003) or plasma radio emission (Mel'nik et al. 1999; Kontar 2001). Finally, effects which may lead to hard X-ray spectral flattening (e.g., albedo and non-uniform ionization; see Kontar et al. 2002, 2003; Liu et al. 2009; Su et al. 2009) should also be carefully assessed before reaching conclusions on the value of the crucial parameter E_c, with its attendant implications for the energy content in nonthermal electrons (e.g., Falewicz et al. 2009).

4.6 Temperature Distribution of Thermal Plasma

The thermal free-free (bremsstrahlung) continuum emission (photons s^{-1} keV^{-1}) at photon energy ϵ from an element of plasma of density n (cm^{-3}), temperature T (K) and volume dV is, neglecting factors of order unity,

$$dI(\epsilon) = a \frac{n^2 \, dV}{\epsilon \, T^{1/2}} \exp(-\epsilon/kT), \tag{4.6}$$

where k is Boltzmann's constant and a is a constant. For an extended source, with nonuniform density and temperature, integration of (4.6) over the spatial extent of the source gives

$$I(\epsilon) = \frac{a}{\epsilon} \int_0^\infty \frac{1}{T^{1/2}} \xi(T) \exp(-\epsilon/kT) \, dT, \tag{4.7}$$

where $\xi(T) = n^2 \, dV/dT$ (cm^{-3} K^{-1}) is the *differential emission measure* at temperature T (see (10) of Craig and Brown 1976). As first pointed out by Brown (1974), (4.7) may be written as a Laplace transform with respect to the inverse temperature variable $x = 1/kT$:

$$\frac{k^{1/2}}{a} \epsilon I(\epsilon) = \int_0^\infty e^{-\epsilon x} f(x) \, dx \equiv \mathcal{L}[f(x); \epsilon], \tag{4.8}$$

where $f(x) = \xi(1/kx)x^{-3/2}$ or, equivalently, $\xi(T) = (kT)^{-3/2} f(1/kT)$.

A solution of (4.8) for $f(x)$ (and hence $\xi(T)$) is formally possible for a large variety of (but, it should be noted, not *all*; see Brown and Emslie 1988) forms of $I(\epsilon)$. Even when a solution does exist, however, the solution of (4.8) is not a trivial task. This integral equation is of Fredholm-type (Bertero et al. 1985) and is highly ill-posed, with a large class of solutions $\xi(T)$ corresponding to a given $I(\epsilon)$ when (even very small) uncertainties in $I(\epsilon)$ are taken into account. Mathematically, this extreme ill-posedness arises from the very broad form of the Laplace kernel $\exp(-\epsilon x)$. *Physically*, the problem exists because of the broad range of temperatures T that contribute to the emission at a given photon energy ϵ. Unlike, for example, the bremsstrahlung photon-to-electron inversion problem (see Sect. 4.2), in which only electrons with energy $E > \epsilon$ contribute to the emission at photon energy ϵ (and so the corresponding integral equation is of Volterra type, and so less ill-posed), in the electron-energy-to-temperature problem considered here *all* temperatures T contribute to the emission at energy ϵ (and conversely a source at a single temperature T produces emission at all photon energies).

An early study of the inversion of (4.8), using data from a balloon-borne instrument (Lin and Schwartz 1987), was carried out by Piana et al. (1995). They deduced not only forms of $\xi(T)$ but also (in a one-dimensional geometry) the corresponding conductive flux $F_c(T)$

and its derivative dF_c/dx. However, later work by Prato et al. (2006) examined the relation between $\xi(T)$ and the mean source electron spectrum $\overline{F}(E)$, viz.,

$$\overline{F}(E) = b \int_0^\infty \frac{1}{T^{1/2}} \xi(T) \exp(-E/kT) \, dT. \tag{4.9}$$

This study utilized the Landweber method, which ensures positivity of $\xi(T)$ everywhere—see (4.5) in Sect. 4.2—and which is effective in recovering narrow, δ-function-like forms of the differential emission measure $\xi(T)$. It also showed that the form of $\xi(T)$ deduced from inversion of this (rigorous) equation is much less well-determined than suggested by the earlier work of Piana et al. (1995), which involved inversion of the (inexact) equation (4.6).

The method was applied to three photon spectra emitted during the flares SOL2002-08-21T01:41 (M1.4), SOL2003-11-03T09:55 (X3.9), and SOL2002-07-23T00:35 (X4.8). The photon spectra were first inverted by applying zero-order Tikhonov regularization to recover the form of $\overline{F}(E)$. For the first two events, the recovered $\xi(T)$ was consistent with a roughly isothermal low-temperature plasma plus a very broad form of $\xi(T)$ at high temperatures. However, for the SOL2002-07-23T00:35 (X4.8) event, the reconstruction method produced unacceptably large residuals at low temperatures, consistent with the fact that this same spectrum fails to satisfy the derivative test (Brown and Emslie 1988) necessary for compatibility with a purely thermal interpretation of the event. Observation of optically-thin lines is often used as an alternative approach to infer the DEM of solar plasma (as a review, see Phillips et al. 2008).

5 The Electron Angular Distribution

Flare studies typically derive the properties of accelerated particles in the target region from observations of the radiation spectrum, but such radiation spectra are strongly dependent on the angular distribution of the energetic particles. Consequently, knowledge of both the angular distribution and the energy distribution of energetic particles, as they interact in the solar material, is necessary for understanding the acceleration and transport of particles in flaring regions.

Attempts to measure the angular distribution of the accelerated electrons rely on the fact that an anisotropic ensemble of bremsstrahlung-producing electrons will generate a radiation field that is both polarized and anisotropic. Efforts to measure electron beaming have therefore concentrated on studies of the hard X-ray continuum emission, by looking at either the directivity or the polarization of the emitted radiation. Theoretical studies have considered the evolution of the electron pitch-angle distribution as the particles are transported along magnetic field lines (e.g., Brown 1972; Leach and Petrosian 1981; McTiernan and Petrosian 1990a, 1990b). It is generally expected that, even if the particles are strongly beamed when injected, the net effect of the particle transport through the atmosphere will be to broaden the angular distribution (Holman et al. 2011, this issue). Ideally, the measurements of the electron angular distribution should therefore be performed as a function of both time and space. No such measurements are available as yet. However, those measurements that are available (as discussed below) already indicate some evidence for electron beaming.

The angular distribution of accelerated ions can be studied by measuring the energies and widths of broad γ-ray lines (for details, see Smith et al. 2003). Studies of γ-ray line data from the *Solar Maximum Mission (SMM)* Gamma Ray Spectrometer (GRS) suggest that

protons and α-particles are likely being accelerated in a rather broad angular distribution (Share and Murphy 1997; Share et al. 2002). It is currently still unclear whether electrons and ions are being accelerated (Zharkova et al. 2011, this issue) in a similar fashion or by the same process.

5.1 Early Results

One technique for studying hard X-ray directivity is to look for center-to-limb variations on a statistical basis. Correlations between flare longitude and flare intensity or spectrum reflect the anisotropy of the X-ray emission and hence an associated anisotropy of the energetic electrons. For example, if the radiation is preferably emitted in a direction parallel to the surface of the Sun, then a flare located near the limb will look brighter than the same flare near the disk center. Various statistical studies of X-ray flares at energies below 300 keV reported no significant center-to-limb variation of the observed intensity (e.g., Datlowe et al. 1974; Pizzichini et al. 1974). A statistically significant center-to-limb variation in the shape of the spectra of these events *was* found by Roy and Datlowe (1975), suggesting that perhaps some directivity may be present.

The large sample of flares detected at energies greater than 300 keV by *SMM*/GRS allowed, for the first time, a statistical search for directivity at higher energies. Analysis of these data collected during Solar Cycle 21 provided the first clear evidence for directed emission, with a tendency for the high energy events to be located near the limb (Vestrand et al. 1987; Bai 1988). Bogovalov et al. (1985) and McTiernan and Petrosian (1991) also reported evidence for anisotropies at hard X-ray energies. Observations from *SMM*/GRS during Solar Cycle 22 provided further support for directivity (Vestrand et al. 1991) at energies above 300 keV. However, several high-energy events were also observed near the disk center by a number of different experiments during Cycle 22 (e.g., on *GRANAT* and the *Compton Gamma-ray Observatory, CGRO*). For a summary, see Vilmer 1994; this perhaps suggests a more complex pattern. Li (1995) used data from *SMM* to confirm the general results of Vestrand et al. (1987) and concluded that there was evidence for increasing directivity with increasing energy. Quantifying the magnitude of the directivity from these statistical measurements is difficult. For example, one needs to know the size-frequency distribution for flares as well as the form of the electron distribution to derive the predicted limb fraction (e.g., Petrosian 1985). Furthermore, the results only represent an average for the flare sample. Different flaring regions are not likely to have identical geometries; nor are individual flares likely to have time-independent electron distributions.

Another, more direct, method for studying directivity in individual flares is the stereoscopic technique (Catalano and van Allen 1973). This method compares simultaneous observations made on two spacecraft that view the same flare from different directions. Kane et al. (1998) combined observations from the *Pioneer Venus Orbiter (PVO)* and *ISEE-3* satellites to produce stereoscopic flare observations of 39 flares in the energy range from 100 keV to 1 MeV. While the range of flux ratios measured by Kane et al. (1998) is consistent with the results of statistical studies (Vestrand et al. 1987), the deviations of the ratio from unity show no clear correlation with increasing difference in viewing angles. Later studies concluded that there was no clear evidence for directivity at hard X-ray energies (Kane et al. 1998; Li et al. 1994). Stereoscopic observations tend to suffer from cross-calibration issues between different instruments.

The high quality hard X-ray data from *RHESSI* have opened new opportunities and diagnostic techniques for the study of electron anisotropy in solar flares.
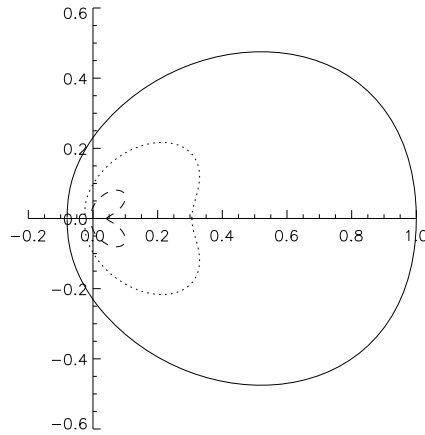
Fig. 16 Polar diagram of the bremsstrahlung cross-section (Gluckstern et al. 1953) for an electron of energy $E = 100$ keV and photon energies $\epsilon = 30$ keV (*solid line*), $\epsilon = 50$ keV (*dotted line*), and $\epsilon = 80$ keV (*dashed line*); the radial coordinate is proportional to the size of the cross-section and the angle from the *x*-axis corresponds to the angle between the incoming electron direction and the line to the observer. Note that at energies $E \gg \epsilon$, the cross-section peaks at $\theta = 0$, while for $E \simeq \epsilon$, the cross-section peaks at $\theta \simeq (30$–$40)°$ (after Massone et al. 2004)

5.2 Anisotropy of X-ray Bremsstrahlung Emission

Using (1.2), it is straightforward to show that the emitted bremsstrahlung in the direction $\mathbf{\Omega}$ toward the observer can be written

$$I(\epsilon, \mathbf{\Omega}) = \frac{\bar{n} V}{4\pi R^2} \int_\epsilon^\infty \int_{\Omega'} \overline{F}(E, \mathbf{\Omega}') Q(\epsilon, E, \theta') \, dE \, d\mathbf{\Omega}', \qquad (5.1)$$

where $Q(\epsilon, E, \theta')$ is the cross-section differential in photon energy ϵ and the angle θ' between the precollision electron direction $\mathbf{\Omega}'$ and the emitted photon direction $\mathbf{\Omega}$, summed over the polarization state of the emitted photon (Gluckstern et al. 1953). The bremsstrahlung cross-section is more angle-dependent for higher photon energies (Fig. 16), which is qualitatively consistent with the findings of the statistical analysis.

In (5.1) the mean source electron flux spectrum has been generalized to the form $\overline{F}(E, \mathbf{\Omega}')$, which takes into account the angular distribution of electrons. If we denote by (θ, ϕ) the polar coordinates of the electron velocity vector $\mathbf{\Omega}'$ relative to the mean direction of the electron velocity distribution (usually the same direction as the guiding magnetic field line), and assume azimuthal symmetry, i.e., no dependence on ϕ, so that $\overline{F}(E, \mathbf{\Omega}') \equiv f(E, \theta)$, and the angle of the mean direction of the electron velocity distribution is θ_0, (5.1) can be written:

$$I(\epsilon) = \frac{\bar{n} V}{4\pi R^2} \int_{E=\epsilon}^\infty \int_{\theta=0}^\pi \int_{\phi=0}^{2\pi} Q\left[\epsilon, E, \theta'(\theta, \phi; \theta_0)\right] f(E, \theta) \sin\theta \, d\phi \, d\theta \, dE, \qquad (5.2)$$

where the directivity angle θ' between electron and photon directions is given by $\cos\theta' = \cos\theta \cos\theta_0 + \sin\theta \sin\theta_0 \cos\phi$. If we now define:

$$K_0(\epsilon, E, \theta) = \int_{\phi=0}^{2\pi} Q\left[\epsilon, E, \theta'(\theta, \phi; \theta_0)\right] d\phi, \qquad (5.3)$$
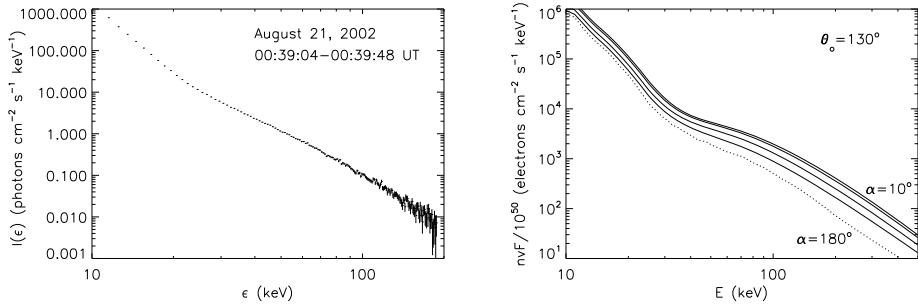
Fig. 17 *Left:* photon flux spectrum. *Right:* regularized electron flux spectra corresponding to $\theta_0 = 130°$ (angle between an observer and the electron beam direction) and (from top to bottom) $\alpha = 10°$, $30°$, $60°$, $90°$, $180°$. The choice of $\theta_0 = 130°$ is justified by the fact that this is the value corresponding to a vertically downward electron beam at the location of the selected flare (after Massone et al. 2004)

we can write

$$I(\epsilon) = \frac{\bar{n}V}{4\pi R^2} \int_{E=\epsilon}^{\infty} \int_{\theta=0}^{\pi} K_0(\epsilon, E, \theta) f(E, \theta) \sin\theta \, d\theta \, dE. \tag{5.4}$$

Inversion of (5.4) requires construction of the bivariate function $f(E, \theta)$ from knowledge of the (noisy) univariate function $I(\epsilon)$. The problem is significantly more tractable if we make the further assumption that $f(E, \theta)$ is separable in E and θ. We can then choose a particular form for the angular dependence of $f(E, \theta)$ and reconstruct the part of $f(E, \theta)$ that depends only on the electron energy (univariate problem in E) or, analogously, we can assume the E-dependence for $f(E, \theta)$ and recover the θ-dependence (univariate problem in θ).

In Massone et al. (2004), the θ-dependence of $f(E, \theta)$ is a prescribed (normalized) form $g(\theta)/\int_{\Omega'} g(\theta) \, d\Omega'$. Specifically, it was assumed that at all energies the pre-collision electron velocities are uniformly distributed over a solid angle within a cone of half-angle α centered on a direction corresponding to a photon emission direction of θ_0. With such an assumption, (5.4) becomes

$$I(\epsilon) = \frac{\bar{n}V}{4\pi R^2} \int_{E=\epsilon}^{\infty} \overline{K_0}(\epsilon, E) \overline{F}(E) \, dE, \tag{5.5}$$

where

$$\overline{K_0}(\epsilon, E) = \frac{1}{2\pi(1 - \cos\alpha)} \int_{\theta=0}^{\alpha} K_0(\epsilon, E, \theta) \sin\theta \, d\theta. \tag{5.6}$$

Equation (5.5) is formally identical to (2.4). Application of the usual Tikhonov regularization technique to (5.5) then yields the mean source energy spectrum $\overline{F}(E)$.

Massone et al. (2004) applied this analysis to a photon spectrum recorded by the *RHESSI* instrument from SOL2002-08-21T01:41 (M1.4) in the time interval 00:39:04-00:39:48 UT (left panel of Fig. 16). Values for the observation angle θ_0 ranging from 0° to 180°, and for the cone semi-angle α ranging from 10° to 180°, were considered. The results (right panel of Fig. 17) demonstrated clearly that the angular dependence cannot be neglected: use of the anisotropic cross-section yields electron spectra that are significantly different from the ones reconstructed by using the solid-angle-averaged cross-section (corresponding to $\alpha = 180°$). As the electron distribution becomes more anisotropic (decrease in α), the cross-section for
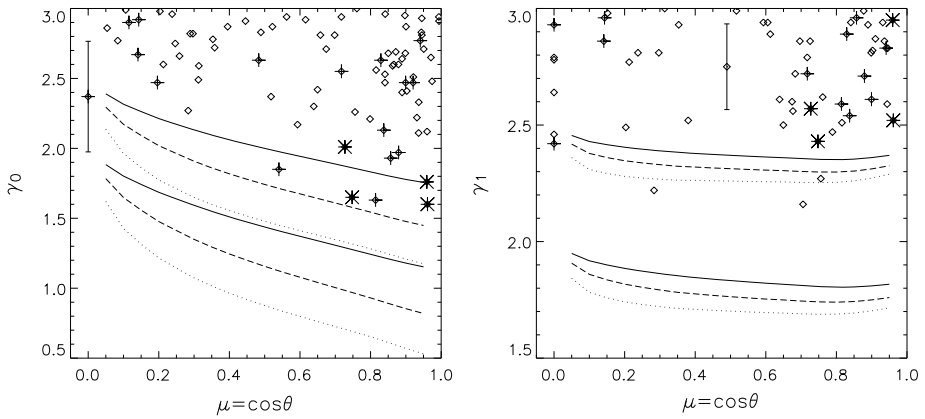
Fig. 18 Spectral index γ_0 (15–20 keV) and γ_1 (20–35 keV) versus cosine μ of heliocentric angle θ. *Vertical error bars* indicate average uncertainties on the values as determined from single power-law fits. *Lines* show the predicted dependency for single power-law primary spectra with spectral indices 2.0, 2.5 and for directivity $\alpha(\mu) = 1, 2, 4$ (*solid*, *dashed*, and *dotted lines* respectively). Flares with a dip in the mean electron distribution are denoted by *stars*; see also Sect. 4.5 (after Kašparová et al. 2007)

emission in the direction of the observer decreases for some parts of the cone and increases for others. The overall effect is a reduction in the cross-section, so that more electrons are required to produce the given photon spectrum. This effect is more pronounced at high energies (see Fig. 17), so the spectrum for small values of α is flatter than for $\alpha = 180°$ (isotropic distribution).

As the viewing angle θ_0 increases (source moves closer to the disk center), the cross-section for emission in direction of the observer in general decreases, especially at high values of E, and accordingly the required electron spectrum increases and also flattens.

5.3 Statistical Results on X-ray Anisotropy

As a result of the heliocentric angle dependence of albedo (Sect. 3), the shape of photon spectra should vary as a function of their position on the solar disk (Bai and Ramaty 1978; Kontar et al. 2006). A statistical analysis of *RHESSI* flares (Kašparová et al. 2007) demonstrates a clear center-to-limb variation of photon spectral indices in the 15–20 keV energy range and a weaker dependency in the 20–50 keV range. The observed spectral variations were found to be consistent with the predictions of albedo-induced spectral index changes (Fig. 18).

Because the number of albedo photons depends on the amount of downward directed primary emission, the characteristics of the albedo component can be used to get an estimate of the anisotropy of the primary hard X-ray emission. In this manner, Kašparová et al. (2007) obtained values for α (the ratio of downward-directed primary emission to observer-directed primary emission) in the 15–20 keV energy range; see Fig. 19. The values of directivity α range from 0.3 to 3; while they imply downward-collimated emission in some cases, overall they are also consistent with isotropic X-ray emission (see also Kontar and Brown 2006b). The model of Leach and Petrosian (1983, Fig. 4) predicts $\alpha \lesssim 3$ at 22 keV for disk-center events.
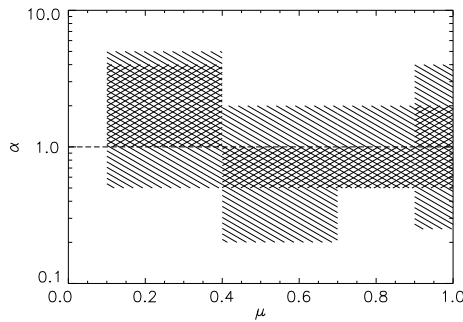
Fig. 19 Directivity at different heliocentric angle μ determined from the distributions of spectral index γ_0 in the 15–20 keV energy range at the limb and a given range of μ. *Cross-hatched areas* show the range of directivity values that are consistent (at the 0.05 significance level) with the hypothesis that the observed distribution at a given range of μ and the modeled distribution are drawn from the same parent distribution; *crossed areas* correspond to the 0.01 significance level. The *dashed line* shows the isotropic case, i.e., $\alpha(\mu) = 1$ (after Kašparová et al. 2007)

5.4 Albedo as a Probe of Electron Angular Distribution

The albedo spectral "contaminant" in fact offers very valuable insight into the anisotropy of the flare fast electron distribution. It does so by providing a view of the hard X-ray flare from behind, like a dentist's mirror. Moreover, the solar albedo "mirror" is spectrally distorting, so that its contribution to the overall spectrum can be distinguished. The observed spectrum in the observer's direction should contain an albedo "bump" feature, the strength of which is an indicator of the degree of downward beaming of the electron distribution. By use of this solar "mirror" we can achieve a degree of knowledge about the directionality of the primary photon distribution, and so the accelerated electron distribution, from single-spacecraft photon spectrometry (Kontar and Brown 2006b).

The required integration over solid angle in (5.1) can be approximated using a bi-directional representation. Invoking axial symmetry about a beam assumed to be perpendicular to the solar surface, we introduce the cross-sections

$$Q(\epsilon, E, \theta_0) = \frac{1}{\cos(\theta_0 - \Delta\theta) - \cos(\theta_0 + \Delta\theta)} \int_{\theta_0 - \Delta\theta}^{\theta_0 + \Delta\theta} Q(\epsilon, E, \theta') \sin(\theta') \, d\theta', \quad (5.7)$$

averaged over $[\theta_0 - \Delta\theta, \theta_0 + \Delta\theta]$ and centered at angle θ_0. We define $Q^F(\epsilon, E) \equiv Q(\epsilon, E, \theta_0 = \theta)$ and $Q^B(\epsilon, E) \equiv Q(\epsilon, E, \theta_0 = 180° - \theta)$, where θ is the heliocentric angle of the source. The electron spectrum $\overline{F}(E, \theta)$ is defined in a similar bi-directional approximation, through introduction of the quantities

$$\overline{F}_{u,d} = \frac{1}{\bar{n}V} \int F_{u,d}(E, \mathbf{r}) n(\mathbf{r}) \, dV \qquad (5.8)$$

for electrons propagating either upward (u) or downward (d) toward the scattering photosphere: $\overline{F}_u(E)$ and $\overline{F}_d(E)$ are the density-weighted volumetric mean flux spectra of electrons directed towards the observer (upward and downward, respectively), also averaged over $\Delta\theta$.

With these assumptions and definitions, the discretized hard X-ray spectrum $\mathbf{I}(\epsilon_i)$; $i = 1, \ldots, N$, accounting both for the primary spectrum $\mathbf{I_o}$ and the reflected spectrum $\mathbf{I_r}$, can be

Fig. 20 *Lower panel:* The recovered mean electron flux spectra defined by (5.8) (*thick lines*) for SOL2002-08-20T08:25 (M3.4) (accumulation time interval 08:25:20-08:25:40 UT). Downward-directed $\overline{F}_d(E)$ (*solid line*) and observer-directed $\overline{F}_u(E)$ (*dashed line*) are shown, with corresponding 2σ errors (*thin lines*). *Upper panel:* electron anisotropy defined as $\overline{F}_d(E)/\overline{F}_u(E)$ with confidence values within the *shaded area* (after Kontar and Brown 2006b)
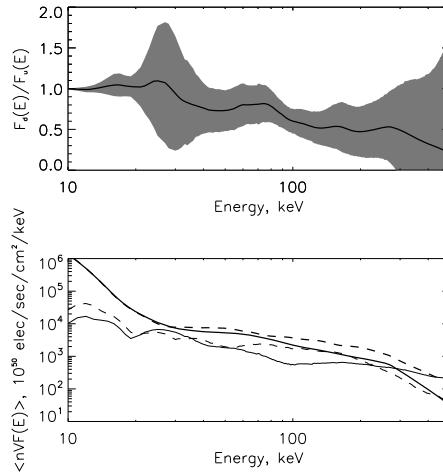
written (Kontar and Brown 2006b)

$$I = I_o + I_r = \left(Q^F + G(\mu)Q^B \quad Q^B + G(\mu)Q^F \right) \begin{pmatrix} \overline{F}_u \\ \overline{F}_d \end{pmatrix}, \tag{5.9}$$

where $\overline{F}_{u,d}(E_j)$; $j = 1, \ldots, M$ are the electron data vectors for downward- and upward-directed electrons, respectively and $Q^{B,F}$ are matrix representations of the kernels of integral equations (5.7). The Green's matrices $G(\mu)$ depend on the heliocentric angle of the source $\mu = \cos\theta$ and have been calculated in Kontar et al. (2006). Kontar and Brown (2006b) have solved the inverse problem (5.9) using first-order Tikhonov regularization method.

Figure 20 shows electron spectral solutions ($\overline{F}_u(E)$, $\overline{F}_d(E)$) for the M3.4 flare SOL2002-08-20T08:25. The results are consistent with isotropy up to $E \approx 100$ keV, with some indication of upward anisotropy above 100 keV. These findings show a near-isotropic distribution (low electron directivity) of the mean electron spectrum of accelerated electrons in solar flares (Kontar and Brown 2006b; Holman et al. 2011, this issue). This strongly contradicts the models with purely collisional transport in solar flares (e.g., Brown 1972; Zharkova and Gordovskyy 2006; Karlický and Kašparová 2009; Holman et al. 2011, this issue).

5.5 X-ray Polarization and Electron Angular Distribution

5.5.1 Model Predictions

The difficulties of statistical and stereoscopic observations for measuring hard X-ray directivity evoke the need for a technique that can measure anisotropies for individual flares. Because the bremsstrahlung cross-section $Q(\epsilon, E, \theta')$ is in general polarization-dependent, polarization is a diagnostic that can, in principle, meet these requirements. Models of nonthermal (e.g., thick-target) hard X-ray production predict a clear and significant polarization signal with polarization levels $>10\%$ for beam-like distributions of electrons (Bai and Ramaty 1978; Brown 1972; Charikov et al. 1996; Emslie and Vlahos 1980; Langer and Petrosian 1977; Leach and Petrosian 1983; Zharkova et al. 1995) and an orientation parallel to the plane containing the guiding magnetic field direction and the direction to the observer. For vertical guiding fields, this orientation direction projects

onto a radial line on the solar disk (Bai and Ramaty 1978; Leach and Petrosian 1983; Zharkova et al. 1995); for other orientations of the guiding field, other polarization vector orientations are possible (Emslie et al. 2008). For strong electron beaming, the polarization degree can reach values up to 60% at energies above 50 keV, or even higher for lower energies (Haug 1972).

All models predict a strong dependence between the observed value of polarization and the viewing angle. The highest polarization degrees are expected for large angles of view, when the line of sight is perpendicular to the magnetic field line. Thus, most theories predict higher polarization for flares located near the solar limb. The direction of the polarization depends on the energy: low energy hard X-rays are negatively polarized whereas, above 350 keV, the sign turns to positive (Bai and Ramaty 1978). Because collisions of beam electrons with ambient particles tend to isotropize the distribution, the highest polarizations (up to 85%) are expected at energies around 100 keV generated in the coronal portions of the top of the flare loop (Leach and Petrosian 1983). Photons observed from the footpoints (in the region of the dense chromosphere) would be polarized only to the level of around 20%. It should also be noted that even thermal models of the hard X-ray source predict a finite polarization of order a few percent, due to thermal gradients in the source (Emslie and Brown 1980). The thermal component, with its rather low polarization, tends to dominate the emission from all flares at energies below about 25 keV.

All these theoretical predictions, while clearly testable, could be criticized on the grounds that the modeling assumptions they contain may be oversimplistic. For example, each model to date assumes a single, simple magnetic field structure about which the emitting electrons spiral. It could be argued that any real flare, particularly one sufficiently large to produce a signal of sufficient strength to enable a polarization measurement, will in all probability contain a mix of structures that would average out any polarization signal present. However, hard X-ray imaging observations in the impulsive phase generally show a fairly simple geometry, consisting of two footpoint sources and perhaps a loop-top source (e.g., Masuda et al. 1995; Sakao et al. 1992). These observations suggest that simple magnetic structures are responsible for the energetic emissions and give support to the possibility that a statistically significant polarization signal could be produced in a large event.

As noted in Sect. 3, and in other places throughout this article, a substantial fraction of the observed hard X-ray flux is backscattered from the solar photosphere, as the so-called *photospherical albedo*. The precise magnitude of this backscattered fraction depends, in part, on the polarization of the primary flux. Further, the reflected component will influence the degree of polarization of the total observed flux, since backscattering will tend to introduce polarization fractions of a few percent at energies below 100 keV (e.g., Bai and Ramaty 1978; Langer and Petrosian 1977). Direct imaging of this albedo patch would place a constraint on the contribution of such backscattered photons to the primary signal. Hudson et al. (2003) have also suggested that Compton scattering in the corona may lead to measurable polarization effects. Clearly, a simultaneous hard X-ray imaging capability (such as that provided by *RHESSI*) represents a major advantage for interpretation of a hard X-ray polarization measurement.

5.5.2 History of Observations

The history of observations of hard X-ray polarization from solar flares is a fascinating subject in its own. The first measurements of X-ray polarization from solar flares (at energies of ∼15 keV) were made by Soviet experimenters using polarimeters aboard the *Intercosmos* satellites. Their polarimeters were made of a hexagonal Be-scatterer surrounded

by six counters located in front of the Be-prism faces. Later versions of the instrument were mounted on a turnable drum to reduce systematical errors. In their initial study, Tindo et al. (1970) reported an average polarization of $P = 40\%$ ($\pm20\%$) for three 1969 X-ray flares: SOL1969-10-20T10:50 (C9.0), SOL1969-10-23T05:15, and SOL1969-10-30T09:30 (M7.3). This study was followed by an analysis of two flares in 1970: SOL1970-10-24T05:41 (M6.4) and SOL1970-11-05T03:21 (X2.3) (Tindo et al. 1972a, 1972b) that showed polarizations of approximately 20% during the impulsive phase. These reports were met with considerable skepticism, on the grounds that they did not adequately allow for proper detector cross-calibration and had limited photon statistics (Brown et al. 1974). Subsequent observations with an instrument on the *OSO-7* satellite seemed to confirm the existence and magnitudes of the polarizations ($\sim10\%$), but these data were compromised by in-flight gain shifts (Nakada et al. 1974). In a later study using a polarimeter on *Intercosmos* 11, Tindo et al. (1976) measured polarizations of only a few percent at ~15 keV for two flares in July 1974. This small but finite polarization is consistent with the predictions for purely thermal emission that contains an admixture of polarized backscattered radiation (Bai and Ramaty 1978).

A decade later, a new polarimeter, designed to measure in the energy range from 5 keV to 20 keV (with about 1.5 keV energy resolution), was flown on the Space Shuttle *Columbia* (Tramiel et al. 1984). This design was based on metallic lithium scattering elements surrounded by gas-proportional counters. Contamination of the Li scattering elements invalidated the pre-flight instrument calibration. An in-flight calibration was performed using two flares near the center of the Sun, under the assumption of null polarization. The upper limits to the polarization derived from this calibration for 6 flares (C and M-classes) were in the range from 2.5% and 12.7% (99% confidence).

Recent measurements at energies below 100 keV have been performed with the SPR-N instrument on the *CORONAS-F* satellite (Zhitnik et al. 2006). The SPR-N instrument included a solar X-ray radiation monitor and a polarimeter capable of detecting signals in the energy ranges of 20–40, 40–60 and 60–100 keV. The polarization detector consisted of a hexahedral Be-scatterer and three pairs of CsI(Na) scintillation detectors located on the faces of the Be prism. With a total effective area ranging between ~0.3 cm^2 at 20 keV to ~1.5 cm^2 at 100 keV, it detected hard X-rays from more than 90 flares between 2001 and 2005. From a sample of 25 solar flares, one could determine the upper limits of the polarization degree from 8 to 40% (3σ). Only for the single case of SOL2003-10-29T20:49 (X10.0), located near Sun center, was a significant polarization level measured: its value increased from 50% (20–40 keV) to greater than 70% (60–100 keV). Although the same flare was observed by *RHESSI*, an independent polarization analysis was not possible because *RHESSI* was located at high magnetic latitude and was experiencing a high level of charged particle events (Suarez-Garcia et al. 2006).

5.5.3 RHESSI Polarization Measurements

RHESSI enables polarization measurements in a wide range of energies from 20 keV to 1 MeV. Its detection system of 9 cylindrical coaxial germanium detectors (Smith et al. 2002), coupled with a satellite rotation every 4 seconds, strongly reduces systematic effects in the polarization measurements. However, the *RHESSI* design is not optimized for studies of polarization and its small effective area for this kind of study, together with the high background contribution, have led to measurements with limited statistical significance.

For the energy range between 20 keV and 100 keV, polarization can be measured using the photons that are scattered into the rear segments of the Ge detectors by a (passive) Be

Fig. 21 Solar flare polarization data from Boggs et al. (2006) for photon energies between 200 keV and 1 MeV. The best fit curve is shown as a *solid line*. The case for 100% polarization is shown as a *dotted line*. The measured polarization for SOL2002-07-23T00:35 (X4.8) is 21% ± 9%. The measured polarization for SOL2003-10-28T11:10 (X17.2) is −11% ± 5%
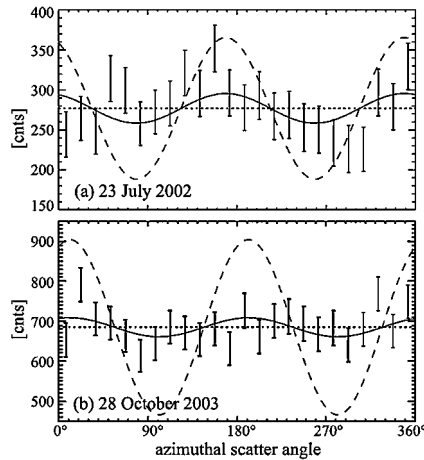
scattering block that is placed between four of the germanium detectors within *RHESSI*'s spectrometer array (McConnell et al. 2002). At energies above ∼100 keV, polarization measurements are performed using the so-called "coincidence mode": photons that Compton-scatter from one Ge detector to another are identified by a suitable coincidence timing window. In this way, one detector plays the role of an *active* scattering element, significantly reducing the background level.

McConnell et al. (2003) reported on a measurement of polarization covering the energy range from 20 keV up to 100 keV performed with the Be scattering block. The initial results from an analysis of SOL2002-07-23T00:35 (X4.8) showed evidence for polarization at a level of $15 ± 4$%. The measured polarization angle (as measured counterclockwise from solar west) was $\Psi = 79°$ ($±5°$), implying that the polarization vector is inclined ∼64° with respect to the radial direction at the flare site. While the magnitude of the observed polarization is broadly consistent with the prediction of solar flare models which invoke the precipitation of a nonthermal electron beam into a dense chromospheric target, the orientation of the polarization vector is somewhat surprising. Emslie et al. (2008) suggest that the orientation of the polarization vector in this case could be explained by a tilt of the flaring loop with respect to the local vertical. Such a tilt is also consistent with gamma-ray line observations for this flare (Smith et al. 2003). Unfortunately, recent analysis of these data (McConnell et al. 2007) suggests that at least a part of the reported signal may be a result of systematic effects in the data analysis, underscoring the difficulty of making reliable polarization measurements.

Using the *RHESSI* coincidence mode, two results have been recently published for energies above 100 keV. The first one (see Fig. 21) describes the polarization measurements of two X-class solar flares, one located close to the solar limb and the other close to the center of the disk (Boggs et al. 2006). The energy range selected was between 200 keV and 1 MeV. The polarization degrees found were 21% ± 10% and −11% ± 5% in 1σ respectively. Assuming that the measured polarization was significant in each case, they measured a radial polarization direction for the flare close to the solar center, and an azimuthal direction for the flare near the limb. The levels of polarization, as well as their directions, are consistent with beamed electron distribution models (Bai and Ramaty 1978) and contrary to the results using the albedo method (Kontar and Brown 2006b; Kašparová et al. 2007). However, the level of inconsistency with more isotropic distributions is rather weak. Given that a report of GRB (gamma-ray burst) polarization by this same team

has been met with considerable skepticism in the literature, one might also question these flare results. It should be noted, however, that the flare analysis differed significantly from the GRB analysis and has not been contested in the literature.

The second study (see Fig. 22) applies the coincidence method to the impulsive phase of seven solar flares in the 100 keV to 350 keV energy range (Suarez-Garcia et al. 2006). The flare sample consisted of six X-class (from X1.4 to X8.4) flares and one M7.0-class flare located either on the limb or in the outer part of the solar disc. Values for the polarization degree were 2% and 54%. The lowest degree of polarization obtained was found to be fully compatible with a 0% polarization measurement. The highest degree of polarization, which was the most statistically significant of the seven results obtained, was found to be 2.6 sigma away from 0. The angles of polarization Ψ were distributed between 35° and 85° independent of the flare location, contrary to both the results mentioned in Boggs et al. (2006), and to the expectation based on simple geometrical modeling. Additional attempts to correlate various parameters (e.g., polarization level, polarization angle, heliocentric angle, footpoint orientation, flare intensity) were also inconclusive. The results were compared with the theoretical predictions from Bai and Ramaty (1978) and Leach and Petrosian (1983) and with the 0% polarization hypothesis. The χ^2 analysis allowed only for rejection (90% of confidence) of one of the models from Leach and Petrosian (1983). In this model, predicting very high polarization values up to 85%, the magnetic field strength is constant along the loop and the electrons spiral at pitch angles close to 90°. Due to the statistical uncertainties, for the rest of the models the χ^2 values were very close to unity, making it impossible to distinguish between them. The polarization amplitudes measured by both Boggs et al. (2006) and Suarez-Garcia et al. (2006) are combined in Fig. 23 with diamonds and filled circles, respectively.

The results to date do not yet provide unambiguous evidence for solar flare polarization at hard X-ray energies. It is clear, however, that such data would constitute a unique probe into the electron acceleration process in solar flares, providing new constraints on theoretical models and allowing for more detailed studies of the acceleration processes and geometries.

6 The Electron Spatial Distribution

Hard X-ray imaging spectroscopy is a powerful tool with which to explore the underlying physics of particle acceleration and transport in solar flares, and has been a central component of the *RHESSI* concept since its beginnings.

6.1 Early Results

In its most basic form, imaging spectroscopy involves simply constructing and comparing two-dimensional (count) maps of the source for different energy bands. The earliest imaging of solar hard X-ray sources was carried out using the Hard X-ray Imaging Spectrometer (HXIS) (van Beek et al. 1980) on *SMM*. This instrument provided imaging information between 3.5 and 30 keV though the use of an array of subcollimator-defining grids; it had an angular resolution of 8 arcsec over a 160 arcsec field of view, and 32 arcsec over a wider, 444 arcsec field. Hoyng et al. (1981a) showed that the hard X-ray emission in SOL1980-04-07T01:07 (M4) was located "in two patches;" the patch with the harder spectrum "coincided with the brightest Hα emission." On the other hand, in SOL1980-04-10T09:23 (M4), the hard X-ray emission was "concentrated in a looplike structure, with the softer spectrum at the top of the loop and the harder spectrum in the legs, thus indicating preference for
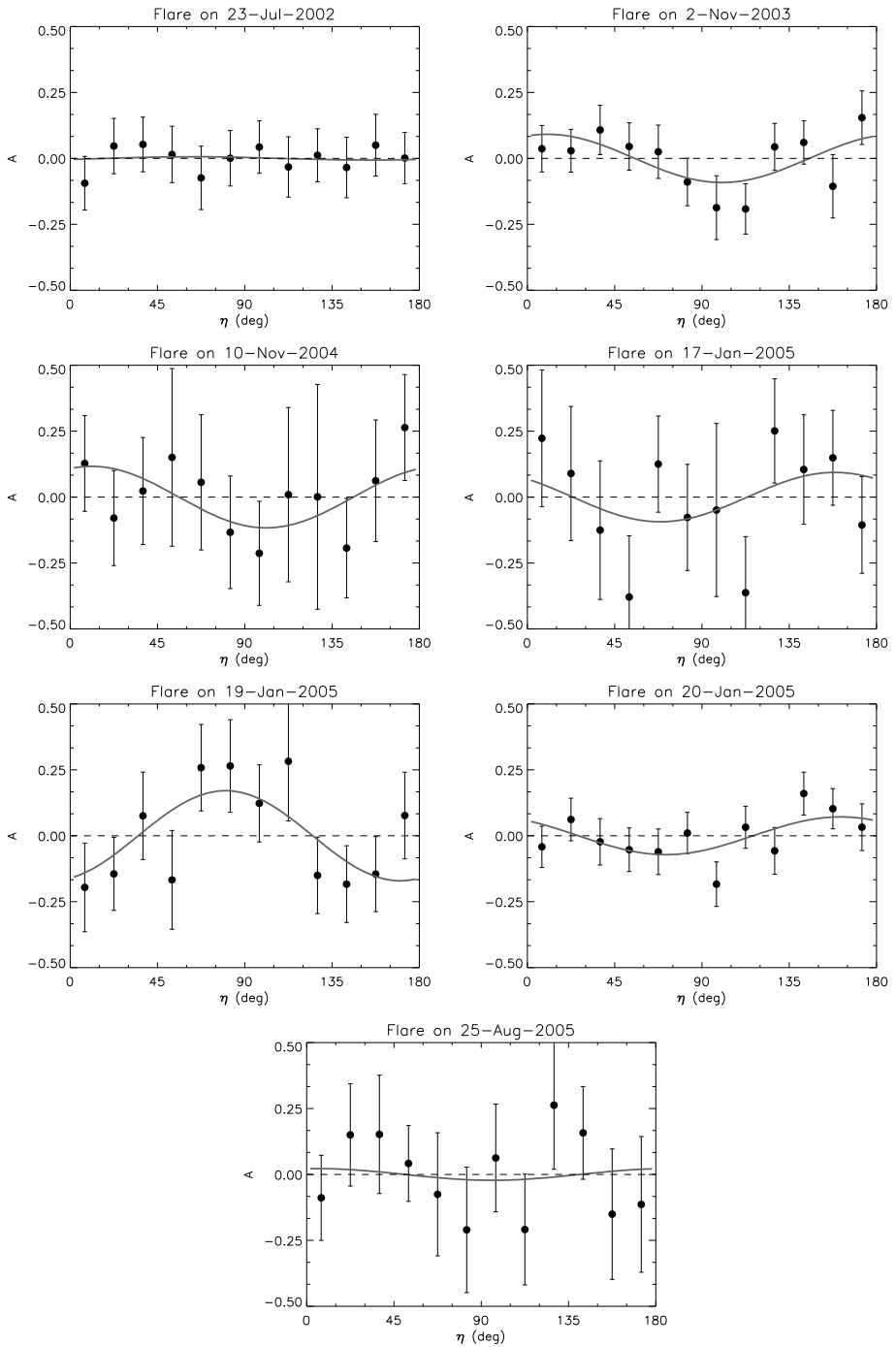
Fig. 22 Solar flare polarization data from Suarez-Garcia et al. (2006) for photon energies between 100 and 350 keV. The best fit curve is shown as a *solid line*. The best case for polarization is from SOL2005-01-19T08:22 (X1.3), where a polarization value of 54% ± 21% was measured
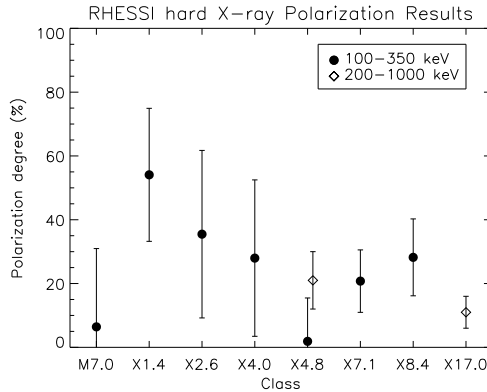
Fig. 23 Results on the absolute value of the degree of hard X-ray polarization above 100 keV achieved with *RHESSI* (1σ errors). The *diamonds* and the *filled circles* correspond to two independent measurements (see text for references). From low to high flare class (left to right) the flares represented are: SOL2005-08-25T04:40 (M6.4), SOL2005-01-19T08:22 (X1.3), SOL2004-11-10T02:13 (X2.5), SOL2005-01-17T09:52 (X3.8), SOL2002-07-23T00:35 (X4.8) (two measurements), SOL2005-01-20T07:01 (X7.1), SOL2003-11-02T17:25 (X8.3), and SOL2003-10-28T11:10 (X17.2). None of these results are significant at a level of greater than 3σ, suggesting that higher quality data are still needed

the thick-target model of hard X-ray production." Hoyng et al. (1981b) studied the hard X-ray emission from a large two-ribbon flare SOL1980-05-21T20:50 (X1) and concluded that the higher-energy (16–30 keV) emission originated in "separate locations of ∼8 arcsec width, coinciding in position with Hα flare kernels," while the softer (3.5–8 keV) emission originated from a "broader region in between."

Treating these observations as evidence for a hot coronal region (Krucker et al. 2008; Tomczak 2009) produced by the primary energy release process, and electron precipitation from this primary acceleration region into the dense chromosphere, Machado et al. (1982) studied the energetics of SOL1980-04-10T09:23 (M4) and concluded that "only a fraction of the total flare energy" was present in the accelerated electrons. Duijveman et al. (1982) continued the study of this event, in addition to SOL1980-05-21T20:50 (X1) and SOL1980-11-15T15:53 (X1). By comparing the energy in the accelerated electrons with an estimate of the thermal conductive flux out of the hot coronal acceleration region, they concluded that "a large fraction of the dissipated flare power has to go into electron acceleration."

The Solar X-ray Telescope (SXT) instrument (Takakura et al. 1983) on the *Hinotori* satellite used the rotating modulation collimator (RMC) technique with two pairs of rotating grids to make hard X-ray images (Oda et al. 1976); the FWHM angular resolution was ∼30 arcsec. Tsuneta et al. (1983, 1984) report observations of a near-limb flare, SOL1981-05-13T06:10 (X1.5), which exhibited a diffuse hard X-ray source situated some 40,000 km above the photosphere. Takakura et al. (1986) reported that a hard X-ray (20–40 keV range) image for the impulsive component of SOL1982-02-22T04:44 (M2.7) was an extended source elongated along the solar limb with a source height of 7,000 km. Tsuneta et al. (1983) also report imaging hard X-ray observations of SOL1981-07-20T14:41 (M5.5), for which "each hard X-ray source in the initial phase coincides with each Hα bright region," further evidence for a thick-target interpretation of the hard X-ray emission at such energies.

In contrast to the RMC technique used by *Hinotori* and *RHESSI*, the Hard X-ray Telescope (HXT) instrument on *Yohkoh* (Kosugi et al. 1991) used information from 64 pairs

of occultation grids; each pair of grids yields a single Fourier component of the source. The FWHM resolution achievable was ∼8 arcsec. Matsushita et al. (1992), using observations of about a hundred flares observed with the *Yohkoh*/HXT, reported that, on average, the hard X-ray source height "decreased with increasing X-ray energy," consistent with the deeper penetration of higher-energy electrons (e.g., Brown and McClymont 1975; Emslie 1978, 1981). With nine RMC components, an angular resolution down to ∼ 2 arcsec, and high spectral resolution, the information available from *RHESSI* (Lin et al. 2002) is far superior for imaging spectroscopy studies.

6.2 Imaging Spectroscopy with *RHESSI*

One of the earliest results using *RHESSI* imaging spectroscopy data was by Aschwanden et al. (2002); see also Krucker and Lin (2002), who analyzed hard X-ray source height as a function of energy, improving the previous statistical analysis (Matsushita et al. 1992). With the superior data available from *RHESSI*, Aschwanden et al. (2002) were able to determine accurate source locations as a function of photon energy for the single event SOL2002-02-20T11:07 (C7.5), rather than a statistical average for an ensemble of events used by Matsushita et al. (1992). This was done by determining the centroid location of a circular Gaussian forward-fit to each of the two clearly resolved footpoints in this event. Then, using thick-target modeling of the expected centroid location vs. photon energy in a plane-parallel-stratified atmosphere model (Brown et al. 2002; Mrozek 2006; Kontar et al. 2008b), they were able to deduce a density vs. height structure for the atmosphere that was consistent with empirical models of flaring atmosphere density.

As mentioned at the outset of this section, imaging spectroscopy is, in principle, straightforwardly accomplished by constructing two-dimensional maps of the source at different energies (e.g., Krucker and Lin 2002; Saint-Hilaire and Benz 2002; Sui et al. 2002; Emslie et al. 2003; Ji et al. 2004; Alexander and Coyner 2006; Jin and Ding 2007; Alexander and Daou 2007; Liu et al. 2008; Dennis and Pernak 2009; Prato et al. 2009; Shao and Huang 2009; Petrosian and Chen 2010). These maps are produced by applying image processing algorithms (e.g., back-projection, CLEAN, Maximum Entropy or Pixon; for details see Hurford et al. 2002) to the temporally modulated fluxes from each of *RHESSI*'s detectors, in which spatial information on the source is encoded. Then,"interesting" regions in the field of view are selected and the intensity in such regions is determined in the map corresponding to each energy range. There results from this a set of intensity-versus-energy profiles, i.e., a count spectrum, for each feature. Using knowledge of the instrument response permits *photon* spectra for each feature to be determined. Finally, the corresponding spatially-resolved *electron* spectra are constructed through forward fitting or by applying regularized spectral inversion methods (e.g., Brown et al. 2006) to the spatially resolved photon spectra. Analysis of the variation of the electron spectrum throughout the target is a powerful diagnostic of the physical processes affecting the bremsstrahlung-producing electrons (see Emslie et al. 2001).

Emslie et al. (2003) performed such a "stacked-image" analysis for different energy bands via an imaging spectroscopy analysis of SOL2002-07-23T00:35 (X4.8). They identified four "interesting" features in the images (Fig. 24) and constructed a count spectrum for each (Fig. 25). They identified one of these features as a "coronal" source, and showed that its spectrum was consistent with a thermal source at a temperature of order 45×10^6 K. The spectra of the other three sources were more power-law-like in form. This, plus their location near the lower altitudes in the flaring structure, led Emslie et al. (2003) to identify these features as chromospheric footpoints.
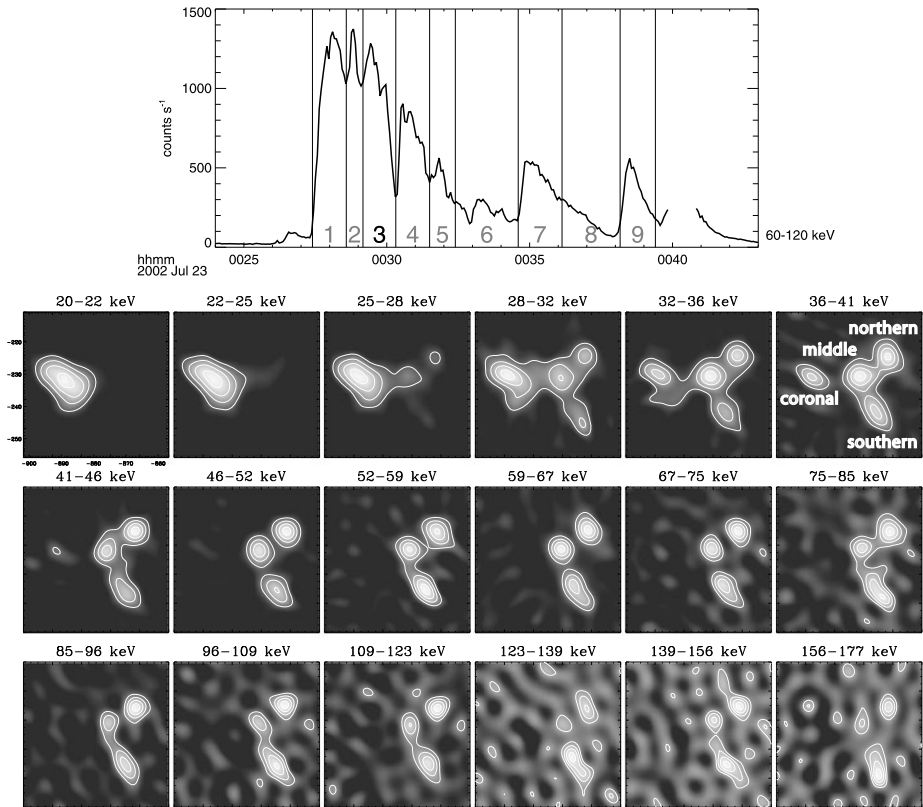
Fig. 24 *Top panel*: time profile for event. *Lower panels*: Images of SOL2002-07-23T00:35 (X4.8) in different count energy channels, for time interval 3 of the event (cf., flux profile in *top panel*). The four main regions in the event are labeled. Since this event was located near the East limb, *structures to the left* are higher in the atmosphere (after Emslie et al. 2003)

Interestingly, the spectra of two of these footpoints (labeled "North" and "South" in Fig. 24), while significantly different and varying with time, maintained a relatively constant *difference* throughout the event. Emslie et al. (2003) interpreted the similar time variation to a magnetic coupling of the two footpoints, and the systematic difference in spectral indices as due to differential spectral hardening associated with an asymmetric location of the electron acceleration region. From the magnitude (∼0.3) of the spectral-index difference, they obtained an estimate of the differential column density between the acceleration region and each of the footpoints. More recently, however, Saint-Hilaire et al. (2008), in a statistical study of some 50 events, have pointed out that such a large intervening column density should in general (but, somewhat ironically, not necessarily in SOL2002-07-23T00:35) produce more emission in the legs of the loop than was observed by *RHESSI*; they conclude that electron precipitation in asymmetric magnetic field geometries is a more reasonable explanation for the observed footpoint spectral differences.

While the above imaging spectroscopy technique appears relatively straightforward to implement, there are a number of difficulties that warrant some commentary. First, for large events, pulse pileup (Datlowe 1976b, 1976a; Smith et al. 2002) is an issue. Pairs of low energy photons arriving nearly simultaneously are detected as a single energy count. Since
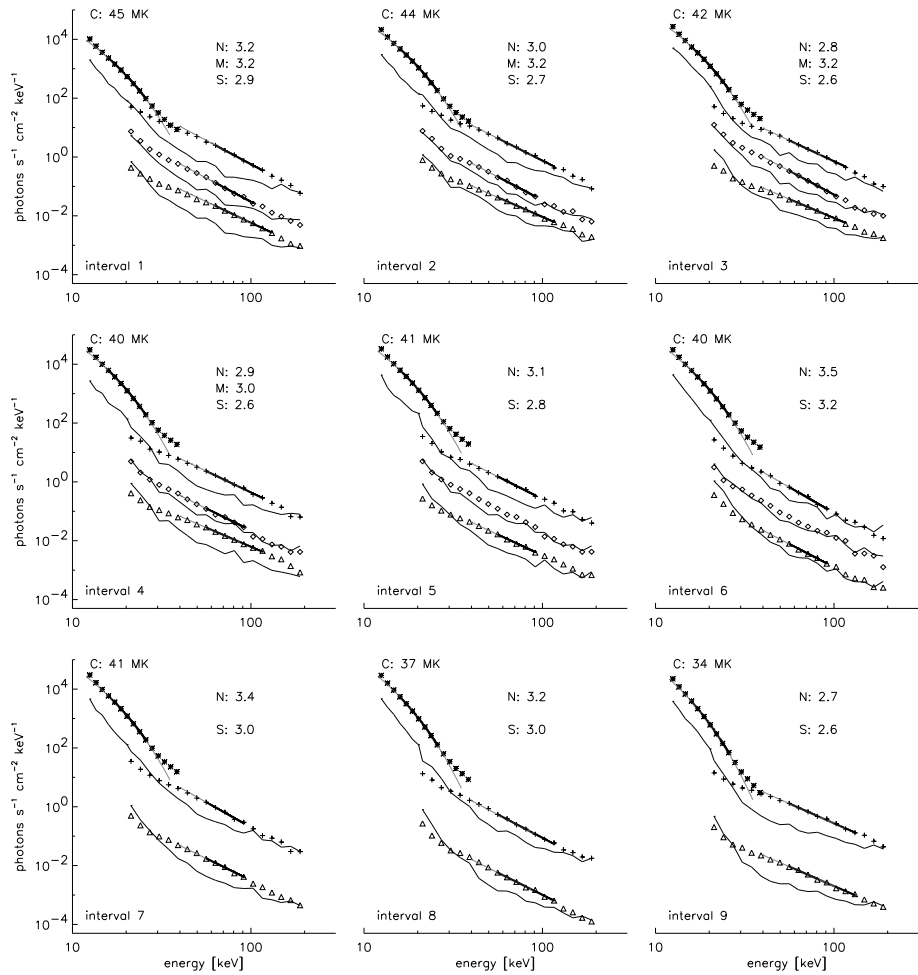
Fig. 25 Spectra for each of the features identified in Fig. 24. For each time interval, the "coronal" source is well-fit to a thermal spectrum with the temperatures shown, and the "footpoint" sources are well-fit by power laws with the spectral indices shown. The spectral indices of the various footpoints vary with time; however, the spectral index *difference* between the "North" and "South" footpoints is relatively constant with time (after Emslie et al. 2003)

the modulation of such counts corresponds to the low energy source, an image made at the higher energy returns a "ghost" image of the low energy source. Second, the dynamic range of *RHESSI* is such that features containing a few percent of the total flux cannot be reliably imaged, so that spectral information in the relevant energy ranges is not reliably recovered. For example, in Emslie et al. (2003) analysis of SOL2002-07-23T00:35, the spectrum of the "coronal" source was determined only at energies ≲40 keV, while the spectrum of the footpoints was determined only at energies ≳30 keV. Only in the relatively narrow energy range from 30 to 40 keV could the spectra of all the features in the source be obtained.

Fig. 26 Construction of electron flux images from measured visibilities. Panel (**a**) shows the "traditional" ▶
approach to image reconstruction, in which the visibility information in count space from each of *RHESSI*'s
nine detectors is used to construct an image based on hard X-ray counts. Note that there is no imposition of
energy smoothing in this process: images in adjacent count energy channels ($q_i \pm \Delta q_i$) can exhibit significant
differences due to count statistics. These differences would be further magnified if the count-based images
were inverted to yield electron images. Panel (**b**) shows the innovative approach of Piana et al. (2007), in
which the energy spectrum for each count visibility (*left panel*) is subjected to a regularized inversion proce-
dure (see, e.g., Piana et al. 2003) to yield the corresponding (smooth) electron spectrum for each visibility.
Once all the electron visibilities have been determined (*right panel*), they can be used to yield electron images
using the same image reconstruction algorithms as used to produce count-based images (Panel (**c**)). These
electron flux images are, by construction, necessarily smooth across electron energy ranges ($E_j \pm \Delta E_j$), and
so are more amenable to further analysis

6.3 Visibilities and Imaging Spectroscopy

It is important to realize that, because of the RMC technique used by *RHESSI*, spatial infor-
mation is encoded in the *RHESSI* data in a distinctive way, namely in rapid time variations
of the detected counts in each of the *RHESSI* subcollimators. Schmahl et al. (2007) have de-
veloped a technique in which the observed temporal modulations produced are interpreted
in terms of a set of *visibilities* (calibrated measurements of specific spatial Fourier compo-
nents of the source distribution). As with image reconstruction in radio interferometry, the
set of visibilities thus determined can then be used to infer the spatial properties of the X-ray
source. It is important to note (1) that visibilities are a "first-order" product of the *RHESSI*
data, and (2) that the data can be used to determine not only the values of the visibilities, but
also their quantitative uncertainties.

Xu et al. (2008) have analyzed a set of ten events, each of which exhibits a rather sim-
ple, single-extended-source, geometry. They performed their imaging spectroscopy analysis
by assuming a parametric form of the source structure (a seven-parameter curved ellipti-
cal Gaussian) and then forward fit not to the actual images themselves, but rather to the
corresponding source *visibilities*. Because both the visibilities and their uncertainties were
determined quantitatively, they were able to deduce not only the best-fit values of the source
parameters, but also the uncertainties on the value of each parameter. Kontar et al. (2008b)
have performed such an analysis with circular Gaussian fits (four parameters) of footpoints
for the SOL2004-01-06T06:29 (M5.8) flare and have measured the sizes and heights of the
hard X-ray sources in a few energy ranges between 18 and 250 keV. The height variations
of footpoint emission with energy and the source size with height have been found with an
unprecedented vertical resolution of ∼150 km at chromospheric heights of 400–1500 km
(cf., Brown et al. 2002; Aschwanden et al. 2002). The interpretation of these findings in
terms of electron transport models is given by Holman et al. (2011, this issue).

One of the major goals of hard X-ray imaging spectroscopy is the determination not
just of the source structure as a function of photon (or count) energy, and hence the vari-
ation of the hard X-ray spectrum throughout the source, but rather of the variation of the
corresponding *electron* spectrum throughout the source. It is the spectral variation of this
electron spectrum that provides the key insight into the physics of electron acceleration and
propagation in solar flares.

Recognizing this, Piana et al. (2007) introduced a new approach to imaging spectroscopy
which is optimized to the distinctive way in which spatial information is encoded in the
RHESSI data. Although it is possible to use the count visibilities determined rather straight-
forwardly from the raw data to construct count images and then proceed to do imaging spec-
troscopy analysis in the "stacked image" manner described above, Piana et al. (2007) point
out that such "traditional" imaging algorithms are completely ineffective in smoothing in

Detector 1 $\{$

	$q_1 \pm \Delta q$	$q_2 \pm \Delta q$	$\cdots$	$q_n \pm \Delta q$
$(u,v)_1$	$V_{1,1}$	$V_{1,2}$	$\cdots$	$V_{1,n}$
$\vdots$	$\vdots$	$\vdots$	$\cdots$	$\vdots$
$(u,v)_{32}$	$V_{32,1}$	$V_{32,2}$	$\cdots$	$\cdot$
$(u,v)_{33}$	$V_{33,1}$	$\cdot$	$\cdots$	$\cdot$
$\vdots$	$\vdots$	$\vdots$	$\cdots$	$\vdots$
$(u,v)_{64}$	$V_{64,1}$	$\cdot$	$\cdots$	$\cdot$
$\vdots$	$\vdots$	$\vdots$	$\cdots$	$\vdots$
$(u,v)_{257}$	$V_{257,1}$	$\cdot$	$\cdots$	$\cdot$
$\vdots$	$\vdots$	$\vdots$	$\cdots$	$\vdots$
$(u,v)_{288}$	$V_{288,1}$	$V_{288,2}$	$\cdots$	$V_{288,n}$

Detector 2 $\{$

Detector 9 $\{$

(a)

$\longrightarrow$ Hard X-ray Image

(b)

	$q_1 \pm \Delta q$	$q_2 \pm \Delta q$	$\cdots$	$q_n \pm \Delta q$
$(u,v)_1$	$V_{1,1}$	$V_{1,2}$	$\cdots$	$V_{1,n}$
$\vdots$	$\vdots$	$\vdots$	$\cdots$	$\vdots$
$(u,v)_{32}$	$V_{32,1}$	$V_{32,2}$	$\cdots$	$\cdot$
$(u,v)_{33}$	$V_{33,1}$	$\cdot$	$\cdots$	$\cdot$
$\vdots$	$\vdots$	$\vdots$	$\cdots$	$\vdots$
$(u,v)_{64}$	$V_{64,1}$	$\cdot$	$\cdots$	$\cdot$
$\vdots$	$\vdots$	$\vdots$	$\cdots$	$\vdots$
$(u,v)_{257}$	$V_{257,1}$	$\cdot$	$\cdots$	$\cdot$
$\vdots$	$\vdots$	$\vdots$	$\cdots$	$\vdots$
$(u,v)_{288}$	$V_{288,1}$	$V_{288,2}$	$\cdots$	$V_{288,n}$

Regularized Inversion $\cdots\cdots\cdots\blacktriangleright$

	$E_1 \pm \Delta E$	$E_2 \pm \Delta E$	$\cdots$	$E_m \pm \Delta E$
$W_{1,1}$	$W_{1,2}$	$\cdots$	$W_{1,m}$	
$\vdots$	$\vdots$	$\cdots$	$\vdots$	
$W_{32,1}$	$W_{32,2}$	$\cdots$		
$W_{33,1}$	$\cdot$	$\cdots$		
$\vdots$	$\vdots$	$\cdots$	$\vdots$	
$W_{64,1}$	$\cdot$	$\cdots$		
$\vdots$	$\vdots$	$\cdots$	$\vdots$	
$W_{257,1}$	$\cdot$	$\cdots$		
$\vdots$	$\vdots$	$\cdots$	$\vdots$	
$W_{288,1}$	$W_{288,2}$	$\cdots$	$W_{288,m}$	

(c)

	$E_1 \pm \Delta E$	$E_2 \pm \Delta E$	$\cdots$	$E_m \pm \Delta E$
	$W_{1,1}$	$W_{1,2}$	$\cdots$	$W_{1,m}$
	$\vdots$	$\vdots$	$\cdots$	$\vdots$
	$W_{32,1}$	$W_{32,2}$	$\cdots$	$\cdot$
	$W_{33,1}$	$\cdot$	$\cdots$	$\cdot$
	$\vdots$	$\vdots$	$\cdots$	$\vdots$
	$W_{64,1}$	$\cdot$	$\cdots$	$\cdot$
	$\vdots$	$\vdots$	$\cdots$	$\vdots$
	$W_{257,1}$	$\cdot$	$\cdots$	$\cdot$
	$\vdots$	$\vdots$	$\cdots$	$\vdots$
	$W_{288,1}$	$W_{288,2}$	$\cdots$	$W_{288,m}$

$\longrightarrow$ Electron Image

the energy direction, with the result that recovered images corresponding to adjacent energy bins can exhibit substantial differences. Further, *RHESSI*'s Fourier-component approach to imaging detects "patterns" of emission, rather than information in a "pixel-by-pixel" for-

mat, so that analysis of a particular sub-region of a source is affected by the signal (and noise) contained in all other features in the source. Piana et al. (2007) therefore argue that imaging spectroscopy analysis using *RHESSI* data is best accomplished through conversion of the temporal modulations in terms of *count visibilities* and subsequent analysis of these count visibilities to obtain information on the electron spectrum in the spatial-frequency (rather than spatial) domain. This leads to a set of *electron visibilities*, which contain all the information on the variation of the electron spectrum throughout the source (albeit as a function of spatial frequency, rather than position). If desired, such electron visibilities can then be used to construct *electron flux maps* using the same algorithms used to convert count visibilities into count maps.

Figure 26 illustrates the essence of this procedure. Visibilities in count space are used to determine the corresponding set of electron visibilities using the Tikhonov regularization technique (Tikhonov 1963) previously used (e.g., Piana et al. 2003) to ascertain spatially-integrated electron spectra $\overline{F}(E)$ from observations of spatially-integrated count (or photon) spectra $I(\epsilon)$ (see Sect. 4.2). Applied to visibilities, the Tikhonov regularization method permits the determination of information on electron fluxes at energies above the maximum count energy observed (Kontar et al. 2004). More importantly, it *forces smoothness in the inferred electron visibility spectra at each point in the spatial frequency domain* and so enhances real features that persist over a relatively wide energy band, while suppressing noise-related features that show up only over a narrow range of energies. The combination of visibility data and the Tikhonov regularization methodology allows the derivation of the most robust information on the spatial structure of the electron flux spectrum image, the key quantity of physical interest.

Piana et al. (2007) have illustrated the power of the electron visibility method by applying it to data obtained near the peak of SOL2002-02-20T11:07 (C7.5). Using visibilities from *RHESSI* RMCs 3 through 9, corresponding to spatial resolutions from $\sim 7''$ to $\sim 183''$, they construct the amplitude and phase of the count visibilities $V(u, v; q)$ (counts $\text{cm}^{-2}\,\text{s}^{-1}\,\text{keV}^{-1}$) as a function of Fourier components (u, v) and count energy q. They then apply the Tikhonov inversion algorithm to construct the corresponding set of electron visibilities $W(u, v; E)$. By construction, these electron visibilities vary smoothly with electron energy E.

Figure 27 shows electron flux images for the illustrative SOL2002-02-20T11:07 (C7.5) event. They show evidence for two footpoints, connected by a "strand" of coronal flux. Because of the inherent smoothness demanded by the regularized algorithm used to construct electron visibilities from count visibilities, the electron flux images vary smoothly with energy. As pointed out by Piana et al. (2007), this contrasts markedly with the behavior in the count images, for which the image in each energy range is independent, so that statistical fluctuations, including those in sidelobes from neighboring features, result in a set of images that do *not* vary smoothly with energy. Inversion of the count spectra obtained from such images leads to amplification of such noise and electron spectra that exhibit large (and most probably) unphysical features.

Three different spatial subregions in the source are highlighted in Fig. 28. Two of these regions correspond to the footpoint sources visible at higher energies and the other one to similarly-sized regions located approximately midway between the two footpoints. The lower panel of Fig. 28 shows the areally-averaged[6] electron-flux spectra (elec-

---

[6]To get the total count spectrum for each region (counts $\text{cm}^{-2}\,\text{s}^{-1}\,\text{keV}^{-1}$), simply multiply the areally-averaged spectrum by the area of that region, viz., $14.4 \times 14.4 = 207.36\ \text{arcsec}^2$ (Footpoint 1), $22.8 \times 9 = 205.2\ \text{arcsec}^2$ (Middle), and $14.4 \times 14.4 = 207.36\ \text{arcsec}^2$ (Footpoint 2), respectively.
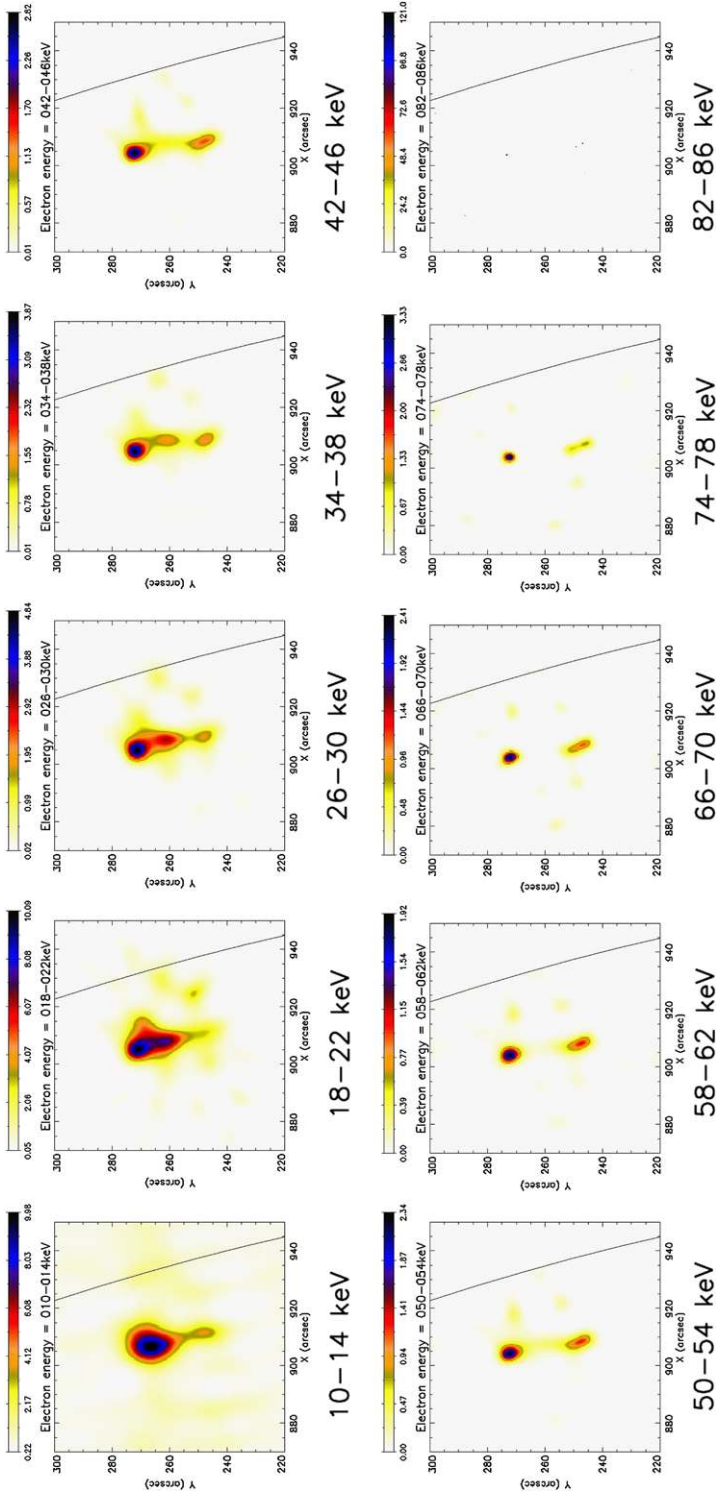
Fig. 27 Electron flux spectral images corresponding to the regularized electron flux spectral visibilities, obtained through application of Bong et al.'s (2006) MEM-NJIT algorithm (after Piana et al. 2007)
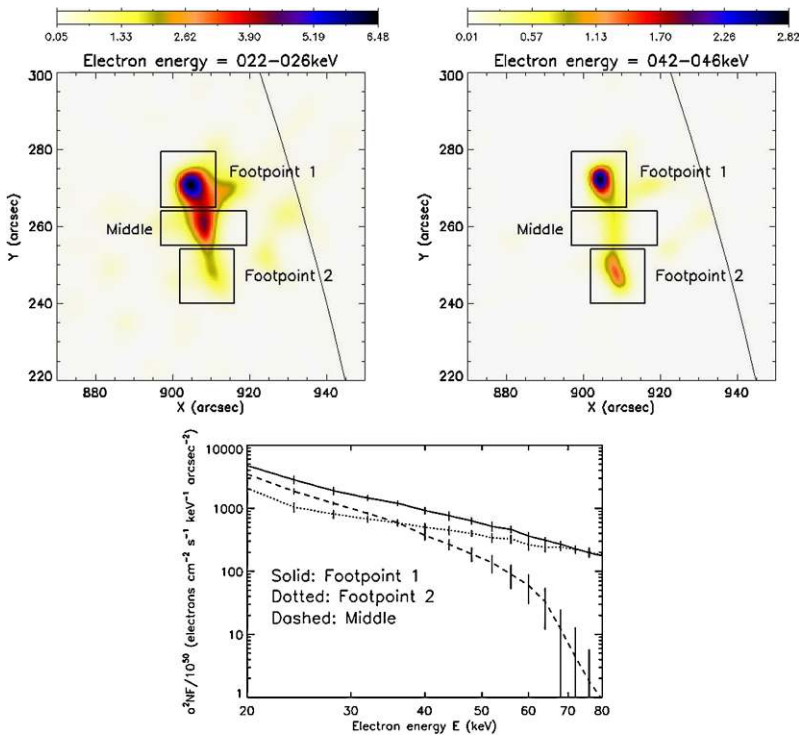
Fig. 28 *Top panels*: Electron images in the energy ranges 22–26 keV and 42–46 keV, respectively. Three sub-regions of interest are labeled on each image. Two of these correspond to bright footpoint-like sources and one to a region midway between the footpoints. *Bottom panel*: Areally-averaged electron flux spectra (electrons $cm^{-2}\,s^{-1}\,keV^{-1}\,arcsec^{-2}$) for each of the three sub-regions shown (after Piana et al. 2007)

trons $cm^{-2}\,s^{-1}\,keV^{-1}\,arcsec^{-2}$), for each of these three subregions. These spectra are sufficiently smooth that significant conclusions regarding the variation of the electron spectrum throughout the source can be made.

7 Summary

7.1 Hard X-ray Emission Processes

With the launch of *RHESSI*, not only have new types of hard X-ray data analysis become possible, but also the in-depth study of X-ray producing processes has been triggered (Sect. 2). The roles of electron-ion and electron-electron bremsstrahlung, free-bound electron-ion emission, and Compton backscatter of primary photons, have been highly scrutinized in view of the unprecedented quality of the *RHESSI* data. Examples include:

- As pointed out in Sect. 2.3, pure electron-ion bremsstrahlung spectra have a spectral index $\gamma \simeq \delta + 1$, for pure electron-electron bremsstrahlung the resulting X-ray spectrum has a significantly shallower photon spectrum, with $\gamma \simeq \delta$. Hence, the importance of the electron-electron bremsstrahlung contribution increases with photon energy and the enhanced emission per electron leads to a flattening of the photon spectrum $I(\epsilon)$ produced

by a given $\overline{F}(E)$, or, equivalently, a steepening of the $\overline{F}(E)$ form required to produce a given $I(\epsilon)$.

- The recent work on the importance of long-neglected free-bound emission by energetic electrons (Sect. 2.2), with its emphasis on emission due to electron capture onto various ionization states of various elements, necessitates further work on the ionization structure of the solar atmosphere and its time dependence during flares.
- The solar atmosphere above an X-ray emitting region can be safely treated as an optically-thin medium, whereas the lower levels of the atmosphere are optically thick for X-rays. X-rays at energies below ∼11 keV are mostly photoelectrically absorbed in the photosphere, while Compton scattering dominates at the energies above. As a result, X-rays emitted downwards can be Compton-backscattered toward the observer; as discussed in Sects. 3.1 and 3.2, they play a major role in the spectral and imaging characteristics of the emission.

7.2 Electron Source Spectrum

The spatially-integrated photon spectrum is a key source of information about the mean electron flux spectrum in solar flares. High-energy-resolution data from *RHESSI* have permitted, for the first time, not only the extraction of basic parameters through forward-fitting the observed spectra (Sect. 4.1), but have also permitted the first reliable model-independent inversion of observed spectra (Sect. 4.2). Although the general form of a large number of nonthermal flare spectra can be adequately approximated by an isothermal Maxwellian for the low-energy component (Sect. 4.6), plus a broken power law for the high-energy component, *RHESSI* data have clearly demonstrated a wealth of features beyond such simple parametric models: the presence of high-energy and low-energy cutoffs (Sects. 4.3 and 4.5), spectral breaks (Sect. 4.4), and the presence of an albedo component leading to "dips" in the mean electron spectrum (Sect. 4.2). The inclusion of an isotropic albedo correction removes the need for low-energy cutoffs and, if low-energy cutoffs exist in the mean electron spectrum, they should be below ∼12 keV (Sects. 3.1 and 4.5).

7.3 Anisotropy

The electron-ion bremsstrahlung emission cross-section is generally anisotropic, with a dipole-like diagram at low energies (Sect. 5). The anisotropy or angular distribution of X-ray emitting electrons can be measured in a number of different ways, and various possibilities have been employed with *RHESSI* data. Parameter-free regularized electron flux spectra, reconstructed by assuming a parameterized form of the electron angular distribution, highlight the need to consider anisotropy in determining the true shape of the electron flux spectrum (Sect. 5.4). A statistical study of center-to-limb variations in the 15–50 keV energy range has shown that an anisotropy factor α, or the ratio of downward and upward directed fluxes, for hard X-ray emission that lies outside the range [0.2, 5] can be rejected with 99% confidence (Sect. 5.3).

The albedo portion of the observed spectrum can be rather effectively used to infer the mean electron flux in two directions simultaneously (Sect. 5.4). The reconstructions of the mean electron spectra in the downward and upward directions suggest that X-ray emitting electrons need not be significantly anisotropic in a broad range of energies from tens of keV to about 200 keV. This imposes significant challenges to solar flare models based on collisional transport; see Fletcher et al. (2011, this issue) and Holman et al. (2011, this issue) for details.

RHESSI has been used to attempt polarization measurements in two different energy bands using two different scattering processes. The results are, however, of limited statistical significance. If real, they would suggest that X-ray polarization above 50 keV is significant (with values up to 50% or more) and that high quality polarization measurements would provide significant constraints on particle acceleration models (Sect. 5.5). The *RHESSI* design is not optimized for studies of polarization, and attempts to measure it have been hampered by the small effective area and the high background contribution. Future progress will require a polarimetric instrument able to measure polarization with errors on the level of 1 to 2%. Such measurements would allow detailed studies of the electron beaming, quantifying its magnitude, and placing significant constraints on the acceleration geometry.

7.4 Spatial Variation of Electron Flux

Imaging spectroscopy results (Sect. 6) from *RHESSI* have (not surprisingly) revealed that the hard X-ray emission from solar flares is far from homogeneous: the centroid of high energy emission moves downward with higher energy, presumably due to the increased penetration of higher energy electrons; coronal sources have radically different spectra than chromospheric footpoints; and even systematic differences exist between different footpoint sources in the same event.

Since *RHESSI* provides spatial information on detected hard X-ray emission through a (Fourier-transform-based) rotating modulation collimator technique, it follows that the highest-fidelity spatial information is contained in the finite number of Fourier components ("visibilities") sampled. Both forward-fit and inversion techniques have been applied to *RHESSI* imaging spectroscopy data, with very positive results, including the first empirical estimates of the density and volume of the electron acceleration region, and the recovery of *electron flux maps* that, by construction, vary smoothly with energy and so provide valuable information on the variation of the emitting electron spectrum throughout the flare source.

References

D. Alexander, A.J. Coyner, Astrophys. J. **640**, 505 (2006). doi:10.1086/500076
D. Alexander, A.G. Daou, Astrophys. J. **666**, 1268 (2007). doi:10.1086/520331
R.C. Alexander, J.C. Brown, Sol. Phys. **210**, 407 (2002). doi:10.1023/A:1022465615445
M.J. Aschwanden, *Physics of the Solar Corona. An Introduction with Problems and Solutions*, 2nd edn. (Pour la Science, Paris, 2005)
M.J. Aschwanden, J.C. Brown, E.P. Kontar, Sol. Phys. **210**, 383 (2002). doi:10.1023/A:1022472319619
T. Bai, Astrophys. J. **334**, 1049 (1988). doi:10.1086/166897
T. Bai, R. Ramaty, Astrophys. J. **219**, 705 (1978). doi:10.1086/155830
M. Bertero, C. DeMol, E.R. Pike, Inverse Probl. **1**, 301 (1985). doi:10.1088/0266-5611/1/4/004

S.E. Boggs, W. Coburn, E. Kalemci, Astrophys. J. **638**, 1129 (2006). arXiv:astro-ph/0510588, doi:10.1086/498930

S.V. Bogovalov, Y.D. Kotov, V.M. Zenchenko, G. Vedrenne, M. Niel, C. Barat, G. Chambon, R. Talon, Sov. Astron. Lett. **11**, 322 (1985)

S.-C. Bong, J. Lee, D.E. Gary, H.S. Yun, Astrophys. J. **636**, 1159 (2006). doi:10.1086/498225

J.C. Brown, Sol. Phys. **18**, 489 (1971)

J.C. Brown, Sol. Phys. **26**, 441 (1972)

J.C. Brown, in *Coronal Disturbances*, ed. by G.A. Newkirk. IAU Symposium, vol. 57 (1974), p. 395

J.C. Brown, M.J. Aschwanden, E.P. Kontar, Sol. Phys. **210**, 373 (2002). doi:10.1023/A:1022469402781

J.C. Brown, A.G. Emslie, Astrophys. J. **331**, 554 (1988). doi:10.1086/166581

J.C. Brown, A.G. Emslie, G.D. Holman, C.M. Johns-Krull, E.P. Kontar, R.P. Lin, A.M. Massone, M. Piana, Astrophys. J. **643**, 523 (2006). doi:10.1086/501497

J.C. Brown, A.G. Emslie, E.P. Kontar, Astrophys. J. Lett. **595**, L115 (2003). doi:10.1086/378169

J.C. Brown, P.C.V. Mallik, Astron. Astrophys. **481**, 507 (2008). arXiv:0706.2823, doi:10.1051/0004-6361:20078103

J.C. Brown, P.C.V. Mallik, Astrophys. J. Lett. **697**, L6 (2009). doi:10.1088/0004-637X/697/1/L6

J.C. Brown, P.C.V. Mallik, N.R. Badnell, Astron. Astrophys. **515**, C1+ (2010). doi:10.1051/0004-6361:20078103e

J.C. Brown, A.N. McClymont, Sol. Phys. **41**, 135 (1975)

J.C. Brown, A.N. McClymont, I.S. McLean, Nature **247**, 448 (1974)

J.C. Brown, R. Turkmani, E.P. Kontar, A.L. MacKinnon, L. Vlahos, Astron. Astrophys. **508**, 993 (2009). arXiv:0909.4243, doi:10.1051/0004-6361/200913145

J.C. Brown, H.F. van Beek, A.N. McClymont, Astron. Astrophys. **41**, 395 (1975)

A. Caspi, R.P. Lin, Astrophys. J. Lett. **725**, L161 (2010). doi:10.1088/2041-8205/725/2/L161

C.P. Catalano, J.A. van Allen, Astrophys. J. **185**, 335 (1973)

J.E. Charikov, A.B. Guzman, I.V. Kudryavtsev, Astron. Astrophys. **308**, 924 (1996)

A.J. Conway, J.C. Brown, B.A.C. Eves, E. Kontar, Astron. Astrophys. **407**, 725 (2003). doi:10.1051/0004-6361:20030897

I.J.D. Craig, J.C. Brown, Astron. Astrophys. **49**, 239 (1976)

I.J.D. Craig, J.C. Brown, *Inverse Problems in Astronomy: A Guide to Inversion Strategies for Remotely Sensed Data* (Adam Hilger, Ltd, Bristol, 1986), p. 159 (Research supported by SERC)

J.L. Culhane, Mon. Not. R. Astron. Soc. **144**, 375 (1969)

J.L. Culhane, L.W. Acton, Mon. Not. R. Astron. Soc. **151**, 141 (1970)

D.W. Datlowe, Space Sci. Instrum. **2**, 523 (1976a)

D.W. Datlowe, Space Sci. Instrum. **2**, 239 (1976b)

D.W. Datlowe, M.J. Elcan, H.S. Hudson, Sol. Phys. **39**, 155 (1974)

B.R. Dennis, Sol. Phys. **100**, 465 (1985)

B.R. Dennis, R.L. Pernak, Astrophys. J. **698**, 2131 (2009). doi:10.1088/0004-637X/698/2/2131

A. Duijveman, P. Hoyng, M.E. Machado, Sol. Phys. **81**, 137 (1982)

A.G. Emslie, Astrophys. J. **224**, 241 (1978). doi:10.1086/156371

A.G. Emslie, Astrophys. J. **245**, 711 (1981). doi:10.1086/158846

A.G. Emslie, Astrophys. J. Lett. **595**, L119 (2003). doi:10.1086/378168

A.G. Emslie, R.K. Barrett, J.C. Brown, Astrophys. J. **557**, 921 (2001). doi:10.1086/322261

A.G. Emslie, H.L. Bradsher, M.L. McConnell, Astrophys. J. **674**, 570 (2008). doi:10.1086/524983

A.G. Emslie, J.C. Brown, Astrophys. J. **237**, 1015 (1980). doi:10.1086/157947

A.G. Emslie, E.P. Kontar, S. Krucker, R.P. Lin, Astrophys. J. Lett. **595**, L107 (2003). doi:10.1086/378931

A.G. Emslie, D.F. Smith, Astrophys. J. **279**, 882 (1984). doi:10.1086/161959

A.G. Emslie, L. Vlahos, Astrophys. J. **242**, 359 (1980). doi:10.1086/158469

R. Falewicz, P. Rudawy, M. Siarkowski, Astron. Astrophys. **500**, 901 (2009). arXiv:0904.1588, doi:10.1051/0004-6361/200811364

F. Fárník, H. Hudson, T. Watanabe, Astron. Astrophys. **320**, 620 (1997)

L. Fletcher et al., Space Sci. Rev. (2011, this issue). doi:10.1007/s11214-010-9701-8

R.L. Gluckstern, M.H. Hull, G. Breit, Phys. Rev. **90**, 1026 (1953). doi:10.1103/PhysRev.90.1026

G. Han, Y. Li, W. Gan, Chin. Astron. Astrophys. **33**, 168 (2009). doi:10.1016/j.chinastron.2009.03.009

I.G. Hannah, E.P. Kontar, O.K. Sirenko, Astrophys. J. Lett. **707**, L45 (2009). arXiv:0911.0314, doi:10.1088/0004-637X/707/1/L45

I.G. Hannah et al., Space Sci. Rev. (2011, this issue). doi:10.1007/s11214-010-9705-4

E. Haug, Sol. Phys. **25**, 425 (1972)

E. Haug, Sol. Phys. **45**, 453 (1975)

E. Haug, Astron. Astrophys. **218**, 330 (1989)

E. Haug, Astron. Astrophys. **326**, 417 (1997)

D. Heristchi, Astrophys. J. **311**, 474 (1986). doi:10.1086/164787

G.D. Holman, Astrophys. J. **586**, 606 (2003). doi:10.1086/367554

G.D. Holman, M.J. Aschwanden, H. Aurass, M. Battaglia, P.C. Grigis, E.P. Kontar, W. Liu, G. Mann, P. Saint-Hilaire, E.J. Schmahl, V.V. Zharkova, Space Sci. Rev. (2011, this issue). doi:10.1007/s11214-010-9680-9

G.D. Holman, L. Sui, R.A. Schwartz, A.G. Emslie, Astrophys. J. Lett. **595**, L97 (2003). doi:10.1086/378488

P. Hoyng, A. Duijveman, A. Boelee, C. de Jager, M. Galama, R. Hoekstra, J. Imhof, H. Lafleur, M.E. Machado, R. Fryer, Astrophys. J. Lett. **244**, L153 (1981a). doi:10.1086/183501

P. Hoyng, A. Duijveman, M.E. Machado, D.M. Rust, Z. Svestka, A. Boelee, C. de Jager, K.T. Frost, H. Lafleur, G.M. Simnett, H.F. van Beek, B.E. Woodgate, Astrophys. J. Lett. **246**, L155+ (1981b). doi:10.1086/183574

G. Huang, Sol. Phys. **257**, 323 (2009). doi:10.1007/s11207-009-9381-2

H.S. Hudson, G.J. Hurford, J.C. Brown, Sol. Phys. **214**, 171 (2003)

G.J. Hurford, E.J. Schmahl, R.A. Schwartz, A.J. Conway, M.J. Aschwanden, A. Csillaghy, B.R. Dennis, C. Johns-Krull, S. Krucker, R.P. Lin, J. McTiernan, T.R. Metcalf, J. Sato, D.M. Smith, Sol. Phys. **210**, 61 (2002). doi:10.1023/A:1022436213688

H. Ji, H. Wang, E.J. Schmahl, Y. Qiu, Y. Zhang, Astrophys. J. **605**, 938 (2004). doi:10.1086/382583

M. Jin, M.D. Ding, Astron. Astrophys. **471**, 705 (2007). doi:10.1051/0004-6361:20077202

C.M. Johns, R.P. Lin, Sol. Phys. **142**, 219 (1992a)

C.M. Johns, R.P. Lin, Sol. Phys. **137**, 121 (1992b)

S.R. Kane, K. Hurley, J.M. McTiernan, M. Boer, M. Niel, T. Kosugi, M. Yoshimori, Astrophys. J. **500**, 1003 (1998). doi:10.1086/305738

M. Karlický, J. Kašparová, Astron. Astrophys. **506**, 1437 (2009). arXiv:0909.0146, doi:10.1051/0004-6361/200912616

J. Kašparová, M. Karlický, E.P. Kontar, R.A. Schwartz, B.R. Dennis, Sol. Phys. **232**, 63 (2005). arXiv:astro-ph/0508636, doi:10.1007/s11207-005-1581-9

J. Kašparová, E.P. Kontar, J.C. Brown, Astron. Astrophys. **466**, 705 (2007). arXiv:astro-ph/0701871, doi:10.1051/0004-6361:20066689

H.W. Koch, J.W. Motz, Rev. Mod. Phys. **31**, 920 (1959). doi:10.1103/RevModPhys.31.920

E.P. Kontar, Sol. Phys. **202**, 131 (2001)

E.P. Kontar, J.C. Brown, Adv. Space Res. **38**, 945 (2006a). arXiv:astro-ph/0508418, doi:10.1016/j.asr.2005.09.029

E.P. Kontar, J.C. Brown, Astrophys. J. Lett. **653**, L149 (2006b). arXiv:astro-ph/0611170, doi:10.1086/510586

E.P. Kontar, J.C. Brown, A.G. Emslie, R.A. Schwartz, D.M. Smith, R.C. Alexander, Astrophys. J. Lett. **595**, L123 (2003). doi:10.1086/378172

E.P. Kontar, J.C. Brown, G.K. McArthur, Sol. Phys. **210**, 419 (2002). doi:10.1023/A:1022494318540

E.P. Kontar, E. Dickson, J. Kašparová, Sol. Phys. **252**, 139 (2008a). arXiv:0805.1470, doi:10.1007/s11207-008-9249-x

E.P. Kontar, A.G. Emslie, A.M. Massone, M. Piana, J.C. Brown, M. Prato, Astrophys. J. **670**, 857 (2007). arXiv:0707.4225, doi:10.1086/521977

E.P. Kontar, A.G. Emslie, M. Piana, A.M. Massone, J.C. Brown, Sol. Phys. **226**, 317 (2005). arXiv:astro-ph/0409691, doi:10.1007/s11207-005-7150-4

E.P. Kontar, I.G. Hannah, A.L. MacKinnon, Astron. Astrophys. **489**, L57 (2008b). arXiv:0808.3334, doi:10.1051/0004-6361:200810719

E.P. Kontar, N.L.S. Jeffrey, Astron. Astrophys. **513**, L2+ (2010). arXiv:1003.0884, doi:10.1051/0004-6361/201014066

E.P. Kontar, A.L. MacKinnon, R.A. Schwartz, J.C. Brown, Astron. Astrophys. **446**, 1157 (2006). arXiv:astro-ph/0510167, doi:10.1051/0004-6361:20053672

E.P. Kontar, M. Piana, A.M. Massone, A.G. Emslie, J.C. Brown, Sol. Phys. **225**, 293 (2004). arXiv:astro-ph/0409688, doi:10.1007/s11207-004-4140-x

A.A. Korchak, Sov. Astron. **11**, 258 (1967)

T. Kosugi, S. Masuda, K. Makishima, M. Inda, T. Murakami, T. Dotani, Y. Ogawara, T. Sakao, K. Kai, H. Nakajima, Sol. Phys. **136**, 17 (1991)

J. Kotoku, K. Makishima, Y. Matsumoto, M. Kohama, Y. Terada, T. Tamagawa, Publ. Astron. Soc. Jpn. **59**, 1161 (2007). arXiv:0708.0057

S. Krucker, M. Battaglia, P.J. Cargill, L. Fletcher, H.S. Hudson, A.L. MacKinnon, S. Masuda, L. Sui, M. Tomczak, A.L. Veronig, L. Vlahos, S.M. White, Astron. Astrophys. Rev. **8** (2008). doi:10.1007/s00159-008-0014-9

S. Krucker, R.P. Lin, Sol. Phys. **210**, 229 (2002). doi:10.1023/A:1022469902940

T.A. Kucera, P.J. Love, B.R. Dennis, G.D. Holman, R.A. Schwartz, D.M. Zarro, Astrophys. J. **466**, 1067 (1996). doi:10.1086/177576

E. Landi, G. Del Zanna, P.R. Young, K.P. Dere, H.E. Mason, M. Landini, Astrophys. J. Suppl. Ser. **162**, 261 (2006). doi:10.1086/498148

M. Landini, B.C. Monsignori Fossi, R. Pallavicini, Sol. Phys. **29**, 93 (1973)

S.H. Langer, V. Petrosian, Astrophys. J. **215**, 666 (1977)

J. Leach, V. Petrosian, Astrophys. J. **251**, 781 (1981). doi:10.1086/159521

J. Leach, V. Petrosian, Astrophys. J. **269**, 715 (1983). doi:10.1086/161081

P. Li, Astrophys. J. **443**, 855 (1995). doi:10.1086/175575

P. Li, K. Hurley, C. Barat, M. Niel, R. Talon, V. Kurt, Astrophys. J. **426**, 758 (1994). doi:10.1086/174112

R.P. Lin, B.R. Dennis, G.J. Hurford, D.M. Smith, A. Zehnder, P.R. Harvey, D.W. Curtis, D. Pankow, P. Turin, M. Bester, A. Csillaghy, M. Lewis, N. Madden, H.F. van Beek, M. Appleby, T. Raudorf, J. McTiernan, R. Ramaty, E. Schmahl, R. Schwartz, S. Krucker, R. Abiad, T. Quinn, P. Berg, M. Hashii, R. Sterling, R. Jackson, R. Pratt, R.D. Campbell, D. Malone, D. Landis, C.P. Barrington-Leigh, S. Slassi-Sennou, C. Cork, D. Clark, D. Amato, L. Orwig, R. Boyle, I.S. Banks, K. Shirey, A.K. Tolbert, D. Zarro, F. Snow, K. Thomsen, R. Henneck, A. Mchedlishvili, P. Ming, M. Fivian, J. Jordan, R. Wanner, J. Crubb, J. Preble, M. Matranga, A. Benz, H. Hudson, R.C. Canfield, G.D. Holman, C. Crannell, T. Kosugi, A.G. Emslie, N. Vilmer, J.C. Brown, C. Johns-Krull, M. Aschwanden, T. Metcalf, A. Conway, Sol. Phys. **210**, 3 (2002). doi:10.1023/A:1022428818870

R.P. Lin, R.A. Schwartz, Astrophys. J. **312**, 462 (1987). doi:10.1086/164891

W. Liu, V. Petrosian, B.R. Dennis, G.D. Holman, Astrophys. J. **693**, 847 (2009). arXiv:0805.1055, doi:10.1088/0004-637X/693/1/847

W. Liu, V. Petrosian, B.R. Dennis, Y.W. Jiang, Astrophys. J. **676**, 704 (2008). arXiv:0709.1963, doi:10.1086/527538

M.E. Machado, A. Duijveman, B.R. Dennis, Sol. Phys. **79**, 85 (1982)

P. Magdziarz, A.A. Zdziarski, Mon. Not. R. Astron. Soc. **273**, 837 (1995)

A.M. Massone, A.G. Emslie, E.P. Kontar, M. Piana, M. Prato, J.C. Brown, Astrophys. J. **613**, 1233 (2004). doi:10.1086/423127

A.M. Massone, M. Piana, A. Conway, B. Eves, Astron. Astrophys. **405**, 325 (2003). doi:10.1051/0004-6361:20030569

S. Masuda, T. Kosugi, H. Hara, T. Sakao, K. Shibata, S. Tsuneta, Publ. Astron. Soc. Jpn. **47**, 677 (1995)

K. Matsushita, S. Masuda, T. Kosugi, M. Inda, K. Yaji, Publ. Astron. Soc. Jpn. **44**, L89 (1992)

M.L. McConnell, J.M. Ryan, D.M. Smith, G.J. Hurford, M.D. Fivian, R.P. Lin, A.G. Emslie, W. Hajdas, in *American Astronomical Society Meeting Abstracts*, vol. 210 (2007), p. 93.01

M.L. McConnell, J.M. Ryan, D.M. Smith, R.P. Lin, A.G. Emslie, Sol. Phys. **210**, 125 (2002). arXiv:astro-ph/0209384, doi:10.1023/A:1022413708738

M.L. McConnell, D.M. Smith, A.G. Emslie, G.J. Hurford, R.P. Lin, J.M. Ryan, in *Bulletin of the American Astronomical Society*, vol. 35 (2003), p. 850

J.M. McTiernan, V. Petrosian, Astrophys. J. **359**, 524 (1990a). doi:10.1086/169084

J.M. McTiernan, V. Petrosian, Astrophys. J. **359**, 541 (1990b). doi:10.1086/169085

J.M. McTiernan, V. Petrosian, Astrophys. J. **379**, 381 (1991). doi:10.1086/170513

V.N. Mel'nik, V. Lapshin, E. Kontar, Sol. Phys. **184**, 353 (1999)

R. Morrison, D. McCammon, Astrophys. J. **270**, 119 (1983). doi:10.1086/161102

T. Mrozek, Adv. Space Res. **38**, 962 (2006). doi:10.1016/j.asr.2006.09.003

M.P. Nakada, W.M. Neupert, R.J. Thomas, Sol. Phys. **37**, 429 (1974)

N. Nitta, B.R. Dennis, A.L. Kiplinger, Astrophys. J. **353**, 313 (1990). doi:10.1086/168618

M. Oda, N. Muranaka, M. Matsuoka, S. Miyamoto, Y. Ogawara, Space Sci. Instrum. **2**, 141 (1976)

V. Petrosian, Astrophys. J. **299**, 987 (1985). doi:10.1086/163765

V. Petrosian, Q. Chen, Astrophys. J. Lett. **712**, L131 (2010). arXiv:1002.2673, doi:10.1088/2041-8205/712/2/L131

K.J.H. Phillips, C. Chifor, B.R. Dennis, Astrophys. J. **647**, 1480 (2006). arXiv:astro-ph/0607309, doi:10.1086/505518

K.J.H. Phillips, U. Feldman, E. Landi, *Ultraviolet and X-ray Spectroscopy of the Solar Atmosphere* (Cambridge University Press, Cambridge, 2008)

M. Piana, Astron. Astrophys. **288**, 949 (1994)

M. Piana, M. Bertero, Inverse Probl. **13**, 441 (1997)

M. Piana, J.C. Brown, A.M. Thompson, Sol. Phys. **156**, 315 (1995)

M. Piana, A.M. Massone, G.J. Hurford, M. Prato, A.G. Emslie, E.P. Kontar, R.A. Schwartz, Astrophys. J. **665**, 846 (2007). doi:10.1086/519518

M. Piana, A.M. Massone, E.P. Kontar, A.G. Emslie, J.C. Brown, R.A. Schwartz, Astrophys. J. Lett. **595**, L127 (2003). doi:10.1086/378171

G. Pizzichini, A. Spizzichino, G.R. Vespignani, Sol. Phys. **35**, 431 (1974)

M. Prato, A.G. Emslie, E.P. Kontar, A.M. Massone, M. Piana, Astrophys. J. **706**, 917 (2009). doi:10.1088/0004-637X/706/1/917

M. Prato, M. Piana, J.C. Brown, A.G. Emslie, E.P. Kontar, A.M. Massone, Sol. Phys. **237**, 61 (2006). doi:10.1007/s11207-006-0029-1

W.H. Press, S.A. Teukolsky, W.T. Vetterling, B.P. Flannery, *Numerical Recipes in FORTRAN. The Art of Scientific Computing*, 2nd edn. (Cambridge University Press, Cambridge, 1992)

J.-R. Roy, D.W. Datlowe, Sol. Phys. **40**, 165 (1975)

P. Saint-Hilaire, A.O. Benz, Sol. Phys. **210**, 287 (2002). arXiv:astro-ph/0210023, doi:10.1023/A:1022478300679

P. Saint-Hilaire, S. Krucker, R.P. Lin, Sol. Phys. **250**, 53 (2008). doi:10.1007/s11207-008-9193-9

T. Sakao, T. Kosugi, S. Masuda, M. Inda, K. Makishima, R.C. Canfield, H.S. Hudson, T.R. Metcalf, J.-P. Wuelser, L.W. Acton, Y. Ogawara, Publ. Astron. Soc. Jpn. **44**, L83 (1992)

N. Santangelo, H. Horstman, E. Horstman-Moretti, Sol. Phys. **29**, 143 (1973)

E.J. Schmahl, G.J. Hurford, Sol. Phys. **210**, 273 (2002). doi:10.1023/A:1022484822851

E.J. Schmahl, G.J. Hurford, Adv. Space Res. **32**, 2477 (2003). doi:10.1016/S0273-1177(03)00938-4

E.J. Schmahl, R.L. Pernak, G.J. Hurford, J. Lee, S. Bong, Sol. Phys. **240**, 241 (2007). doi:10.1007/s11207-007-0263-1

R.A. Schwartz, A. Csillaghy, A.K. Tolbert, G.J. Hurford, J. Mc Tiernan, D. Zarro, Sol. Phys. **210**, 165 (2002). doi:10.1023/A:1022444531435

C. Shao, G. Huang, Astrophys. J. **691**, 299 (2009). doi:10.1088/0004-637X/691/1/299

G.H. Share, R.J. Murphy, Astrophys. J. **485**, 409 (1997). doi:10.1086/304407

G.H. Share, R.J. Murphy, J. Kiener, N. de Séréville, Astrophys. J. **573**, 464 (2002). arXiv:astro-ph/0203215, doi:10.1086/340595

D.M. Smith, R.P. Lin, P. Turin, D.W. Curtis, J.H. Primbsch, R.D. Campbell, R. Abiad, P. Schroeder, C.P. Cork, E.L. Hull, D.A. Landis, N.W. Madden, D. Malone, R.H. Pehl, T. Raudorf, P. Sangsingkeow, R. Boyle, I.S. Banks, K. Shirey, R. Schwartz, Sol. Phys. **210**, 33 (2002). doi:10.1023/A:1022400716414

D.M. Smith, G.H. Share, R.J. Murphy, R.A. Schwartz, A.Y. Shih, R.P. Lin, Astrophys. J. Lett. **595**, L81 (2003). arXiv:astro-ph/0306292, doi:10.1086/378173

Y. Su, G.D. Holman, B.R. Dennis, A.K. Tolbert, R.A. Schwartz, Astrophys. J. **705**, 1584 (2009). doi:10.1088/0004-637X/705/2/1584

E. Suarez-Garcia, W. Hajdas, C. Wigger, K. Arzner, M. Güdel, A. Zehnder, P. Grigis, Sol. Phys. **239**, 149 (2006). arXiv:astro-ph/0609778, doi:10.1007/s11207-006-0268-1

L. Sui, G.D. Holman, B.R. Dennis, Astrophys. J. **626**, 1102 (2005). doi:10.1086/430086

L. Sui, G.D. Holman, B.R. Dennis, Astrophys. J. **670**, 862 (2007). doi:10.1086/522198

L. Sui, G.D. Holman, B.R. Dennis, S. Krucker, R.A. Schwartz, K. Tolbert, Sol. Phys. **210**, 245 (2002). doi:10.1023/A:1022417832283

T. Takakura, K. Tanaka, N. Nitta, K. Kai, K. Ohki, Sol. Phys. **107**, 109 (1986)

T. Takakura, S. Tsuneta, N. Nitta, K. Makishima, T. Murakami, Y. Ogawara, M. Oda, K. Ohki, S. Miyamoto, Astrophys. J. Lett. **270**, L83 (1983). doi:10.1086/184075

A.N. Tikhonov, Sov. Math. Dokl. **4**, 1035 (1963)

I.P. Tindo, V.D. Ivanov, S.L. Mandel'Stam, A.I. Shuryghin, Sol. Phys. **14**, 204 (1970)

I.P. Tindo, V.D. Ivanov, S.L. Mandel'Stam, A.I. Shuryghin, Sol. Phys. **24**, 429 (1972a)

I.P. Tindo, V.D. Ivanov, B. Valníček, M.A. Livshits, Sol. Phys. **27**, 426 (1972b)

I.P. Tindo, A.I. Shurygin, W. Steffen, Sol. Phys. **46**, 219 (1976)

F.F. Tomblin, Astrophys. J. **171**, 377 (1972)

M. Tomczak, Astron. Astrophys. **502**, 665 (2009). arXiv:0901.4227, doi:10.1051/0004-6361/200911732

L.J. Tramiel, R. Novick, G.A. Chanan, Astrophys. J. **280**, 440 (1984). doi:10.1086/162010

G. Trottet, N. Vilmer, C. Barat, A. Benz, A. Magun, A. Kuznetsov, R. Sunyaev, O. Terekhov, Astron. Astrophys. **334**, 1099 (1998)

S. Tsuneta, T. Takakura, N. Nitta, K. Makishima, T. Murakami, M. Oda, Y. Ogawara, I. Kondo, K. Ohki, K. Tanaka, Astrophys. J. **280**, 887 (1984). doi:10.1086/162064

S. Tsuneta, T. Takakura, N. Nitta, K. Makishima, T. Murakami, M. Oda, Y. Ogawara, K. Ohki, Sol. Phys. **86**, 313 (1983)

H.F. van Beek, P. Hoyng, B. Lafleur, G.M. Simnett, Sol. Phys. **65**, 39 (1980)

W.T. Vestrand, Sol. Phys. **118**, 95 (1988)

W.T. Vestrand, D.J. Forrest, E.L. Chupp, E. Rieger, G.H. Share, Astrophys. J. **322**, 1010 (1987). doi:10.1086/165796

W.T. Vestrand, D.J. Forrest, E. Rieger, in *International Cosmic Ray Conference*, vol. 3 (1991), p. 69

N. Vilmer, Astrophys. J. Suppl. Ser. **90**, 611 (1994). doi:10.1086/191882

Y. Xu, A.G. Emslie, G.J. Hurford, Astrophys. J. **673**, 576 (2008). doi:10.1086/524184

V.V. Zharkova, J.C. Brown, D.V. Syniavskii, Astron. Astrophys. **304**, 284 (1995)

V.V. Zharkova, M. Gordovskyy, Astrophys. J. **651**, 553 (2006). doi:10.1086/506423

V.V. Zharkova et al., Space Sci. Rev. (2011, this issue). doi:10.1007/s11214-011-9803-y

I.A. Zhitnik, S.V. Kuzin, A.M. Urnov, S.A. Bogachev, F.F. Goryaev, S.V. Shestov, Sol. Syst. Res. **40**, 272 (2006). doi:10.1134/S0038094606040022